Dust-vortex Instability in the Regime of Well-coupled Grains

Surville, Clément ; Mayer, Lucio

Abstract: We present a novel study of dust-vortex evolution in global two-fluid disk simulations to find out if evolution toward high dust-to-gas ratios can occur in a regime of well-coupled grains with low Stokes numbers (St = 10−3 − 4 × 10−2). We design a new implicit scheme in the code RoSSBi, to overcome the short time-steps occurring for small grain sizes. We discover that the linear capture phase occurs self-similarly for all grain sizes, with an intrinsic timescale (characterizing the vortex lifetime) scaling as 1/St. After vortex dissipation, the formation of a global active dust ring is a generic outcome confirming our previous results obtained for larger grains. We propose a scenario in which, regardless of grain size, multiple pathways can lead to local dust-to-gas ratios of about unity and above on relatively short timescales, <105 yr, in the presence of a vortex, even with St = 10−3. When St > 10−2, the vortex is quickly dissipated by two-fluid instabilities, and large dust density enhancements form in the global dust ring. When St < 10−2, the vortex is resistant to destabilization. As a result, dust concentrations occur locally due to turbulence developing inside the vortex. Regardless of the Stokes number, dust-to-gas ratios in the range 1–10, a necessary condition to trigger a subsequent streaming instability, or even a direct gravitational instability of the dust clumps, appears to be an inevitable outcome. Although quantitative connections with other instabilities still need to be made, we argue that our results support a new scenario of vortex-driven planetesimal formation.

DOI: https://doi.org/10.3847/1538-4357/ab3e47

The Astrophysical Journal, 883:176 (21pp), 2019 October 1 https://doi.org/10.3847/1538-4357/ab3e47

Dust-vortex Instability in the Regime of Well-coupled Grains

Clément Surville and Lucio Mayer
Institute for Computational Science, University of Zurich, Winterthurerstrasse 190, 8057 Zurich, Switzerland; clement.surville@physik.uzh.ch
Received 2018 January 23; revised 2019 August 5; accepted 2019 August 24; published 2019 October 3

Abstract

We present a novel study of dust-vortex evolution in global two-fluid disk simulations to find out if evolution toward high dust-to-gas ratios can occur in a regime of well-coupled grains with low Stokes numbers ($St = 10^{-3} - 4 \times 10^{-2}$). We design a new implicit scheme in the code RoSSBi, to overcome the short time-steps occurring for small grain sizes. We discover that the linear capture phase occurs self-similarly for all grain sizes, with an intrinsic timescale (characterizing the vortex lifetime) scaling as $1/St$. After vortex dissipation, the formation of a global active dust ring is a generic outcome confirming our previous results obtained for larger grains. We propose a scenario in which, regardless of grain size, multiple pathways can lead to local dust-to-gas ratios of about unity and above on relatively short timescales, $<10^5$ yr, in the presence of a vortex, even with $St = 10^{-3}$. When $St > 10^{-2}$, the vortex is quickly dissipated by two-fluid instabilities, and large dust density enhancements form in the global dust ring. When $St < 10^{-2}$, the vortex is resistant to destabilization. As a result, dust concentrations occur locally due to turbulence developing inside the vortex. Regardless of the Stokes number, dust-to-gas ratios in the range 1–10, a necessary condition to trigger a subsequent streaming instability, or even a direct gravitational instability of the dust clumps, appears to be an inevitable outcome. Although quantitative connections with other instabilities still need to be made, we argue that our results support a new scenario of vortex-driven planetesimal formation.

Key words: instabilities – methods: numerical – planets and satellites: formation – protoplanetary disks

1. Introduction

The composition of early protoplanetary disks is dominated by a mixture of hydrogen and helium gas. An important but small fraction of the disk mass, a few percent, is comprised of small dust grains with sizes ranging from micrometers to millimeters. These dust grains are responsible for the infrared excess observed in young disk emissions (see, e.g., Gras-Velázquez & Ray 2005; Meyer et al. 2008; Smith et al. 2008; Bryden et al. 2009). This solid component is the building material for pebbles and planetesimals from which planets and other large-size objects may form.

Grain growth models try to explain how small grains become larger, e.g., by sticking or bouncing. However, existing models do not yet fully capture the coupled gas-dust dynamics in the disk. In particular, the drag force exerted on small grains produces a strong mixing with the gas, making it difficult for dust concentrations to arise. Alternatively, if particular gas structures such as vortices appear, it is possible that small grains accumulate in these locations, albeit on different timescales—depending on the grain size. Due to numerical constraints, studies often focus on larger grains that are only weakly coupled to the gas, i.e., grain sizes with Stokes numbers close to unity (Fu et al. 2014; Zhu et al. 2014). Examples of such numerical studies are those aimed at studying two-fluid instabilities that can trigger stronger local dust concentrations, such as the streaming instability (SI; Youdin & Goodman 2005; Johansen & Youdin 2007; Youdin & Johansen 2007; Jacquet et al. 2011; Kowalik et al. 2013; Simon et al. 2016), instabilities resulting from the evolution and dissipation of anticyclonic vortices (Fu et al. 2014; Surville et al. 2016), or, more recently, a broad class of such instabilities occurring in a resonant regime (Hopkins & Squire 2018; Lin & Youdin 2017; Squire & Hopkins 2018), of which SI is an example.

From previous studies, it is unclear whether significant evolution of the dust density distribution can also occur when the grains are small and strongly coupled with the gas. Understanding the dynamics in this regime is important, for example, in validating whether the SI and the gravitational instability can work in tandem as a viable pathway to planetesimal formation (Youdin 2011; Johansen et al. 2012; Simon et al. 2016; Schäfer et al. 2017). While the premise is attractive, the required conditions are restrictive. In particular, the dust must be dominated by weakly coupled particles—with Stokes numbers of order unity so that the back-reaction is strong—and local dust-to-gas ratios of about unity must be already in place. Such restrictions apply in local and global simulations in two and three dimensions (Kowalik et al. 2013; Simon et al. 2016). It has yet to be shown that such conditions can occur for submillimeter (submm) dust grains that are still strongly coupled to the gas.

In this paper we study the dynamics of smaller grains, with Stokes number $St < 10^{-2}$, which is a nearly unexplored territory at the moment. Our study is a follow-up to the investigation of Surville et al. (2016), in which we considered the effect of vortices on dust evolution in global 2D disk simulations. Almost without exception, we found that the dust-to-gas ratio inside vortices would exceed unity and eventually spread out into turbulent, long-lived dust rings. These dust rings might offer the missing link to generate naturally conditions that are favorable to the SI. It is thus crucial to find out if the same multistage evolution of the dust component toward global structures with high dust-to-gas ratios can occur even when the initial grain size is in a regime of small Stokes number. This is not obvious because in our previous results the back-reaction of dust onto gas was shown to play a crucial role in driving the formation of turbulent dust rings after vortex dissipation. We expect the back-reaction to become weaker as

the coupling between the gas and dust becomes stronger at small Stokes numbers.

The vortex instability that develops after the capture of the solids as well as the active dust rings that form eventually after vortex dissipation are a source of diffusion of the dust grains of larger size. They limit the dust-to-gas ratio to 1–10 in the eddies. However, as concerns the small sized well-coupled grains, turbulent diffusion may have an impact on the evolution of the dusty vortex.

The origin of turbulence in the vortex is unclear, and for the moment, the main process could be the elliptical instability of incompressible vortices. This instability, proposed in Lesur & Papaloizou (2009), concerns 3D vortices of aspect ratio lower than 4, with closed streamlines (a consequence of incompressibility). However, it is unclear if such vortices exist in a fully compressible flow. As shown in Surville & Barge (2015), 2D vortices of aspect ratio lower than 4 have open streamlines. As a result, they may resist the elliptical instability in a 3D context, but this has to be confirmed. A step toward such a confirmation is present in Meheut et al. (2010), who found 3D vortices with open streamlines, and vertical motion inside the vortex. Such properties would reduce the efficiency of the instability, and keep the vortex flow laminar.

In this work, the large vortex with which dust is interacting has an aspect ratio close to 6, and will be quiet to hydrodynamical turbulence. We thus propose a study of this category of non-turbulent vortices with open streamlines. We show how dust diffusion generated by the two-fluid interaction is efficient, and how it compares to previous works where turbulent diffusion of dust in elliptical vortices is at play.

The implications of such a study are important not only for investigating possible routes toward planetesimal formation, but also because it would have immediate observational consequences if substructures in the dust component can still be triggered even in the regime of small grains. In other words, addressing this regime can be potentially important for correctly interpreting the infrared observations of T Tauri and debris disks carried out by ALMA as well as by other instruments (Pérez et al. 2014; Brogan et al. 2015; Andrews et al. 2016).

Our new focus on small dust grains poses some significant numerical challenges in a global disk simulation. Numerical integration of the drag force interaction for small grains is indeed demanding because it implies large source terms in the dynamical equations. As these source terms are proportional to the dust density but inverse to the Stokes number, they can develop very steep gradients in dense regions. Any type of a second-order explicit method would require a very small time-step and force the evolution to proceed on the natural timescale of the drag force, i.e., $St/(\Omega_k)$. Therefore we developed a semi-implicit method to circumvent this problem. We show how efficient and accurate this is for the pressureless fluid approximation. This method was used to accomplish the various simulations presented in this paper.

The paper is organized as follows. Section 2 covers the details of the implicit numerical method we used to accurately follow the dynamics of dust under the small Stokes number regime. Section 3 describes the initial conditions of the simulations and the disk model. Section 4 presents the results of the numerical runs and describes the main observations of the evolution of the dusty vortices, in particular, the different main phases of evolution. These phases are detailed and analyzed in the discussion, Section 5, and a novel framework for the evolution paths of dusty disks as a function of grain size is presented. Finally, our summary and perspectives are given in the conclusions, Section 6.

2. Methods: Integration of the Aerodynamical Friction

In this first section, we present the main equations describing the flow of gas and dust in the disk. The dust component is modeled by a pressureless fluid, which is particularly appropriate in the case of well-coupled grains, i.e., for small grains. The two fluids interact via aerodynamical friction, which is a force inversely proportional to the Stokes number of the dust grains, St. As a consequence, the friction process becomes much faster than the other components of the motion, such as the Keplerian rotation and the wave propagation. Following friction with an explicit scheme like a Runge–Kutta integration becomes inaccurate and inefficient as long as the grain sizes are small.

We propose an implicit method that removes the time-step restrictions imposed by the drag, thereby allowing us to default to the usual hydrodynamic time interval used in a single-phase simulation.

2.1. Equations of Coupled Fluids

In order to keep the conservative form of the Euler equations, we consider the momentum of the gas and particle fluids, $\boldsymbol{\mathcal{P}}_g = \sigma_g \boldsymbol{V}_g$ and $\boldsymbol{\mathcal{P}}_p = \sigma_p \boldsymbol{V}_p$, respectively. We caution not to confuse $\boldsymbol{\mathcal{P}}$, which is an momentum in this section, with any pressure. With these quantities, the conservation of movement of gas and particle fluids can be written as

$$\partial_t \boldsymbol{\mathcal{P}}_g = \boldsymbol{\mathcal{A}}_g + \Omega_k(r) St^{-1}\left(\boldsymbol{\mathcal{P}}_p - \frac{\sigma_p}{\sigma_g}\boldsymbol{\mathcal{P}}_g\right), \tag{1}$$

$$\partial_t \boldsymbol{\mathcal{P}}_p = \boldsymbol{\mathcal{A}}_p - \Omega_k(r) St^{-1}\left(\boldsymbol{\mathcal{P}}_p - \frac{\sigma_p}{\sigma_g}\boldsymbol{\mathcal{P}}_g\right), \tag{2}$$

with $\Omega_k(r) \propto r^{\beta_\Omega}$ the Keplerian frequency, so $\beta_\Omega = -3/2$.

In writing this system of equations, we have combined advection terms, Keplerian, and geometrical source terms in unique operators $\boldsymbol{\mathcal{A}}_g$ and $\boldsymbol{\mathcal{A}}_p$ for gas and particles, respectively. Until this point, we have not made any approximation. We now introduce the local dust-to-gas ratio, $\varepsilon = \sigma_p/\sigma_g$, and assume it is quasi-steady over the time period considered, typically the time step of integration. Upon defining the drag frequency, $\omega_p = \Omega_k(r)\ St^{-1}$, we obtain a single equation

$$\partial_t(\boldsymbol{\mathcal{P}}_p - \varepsilon\boldsymbol{\mathcal{P}}_g) = \boldsymbol{\mathcal{A}}_p - \varepsilon\boldsymbol{\mathcal{A}}_g - (1+\varepsilon)\omega_p(\boldsymbol{\mathcal{P}}_p - \varepsilon\boldsymbol{\mathcal{P}}_g). \tag{3}$$

Finally, we introduce the differential quantities $\Delta\boldsymbol{\mathcal{A}} = \boldsymbol{\mathcal{A}}_p - \varepsilon\boldsymbol{\mathcal{A}}_g$, and $\Delta\boldsymbol{\mathcal{P}} = \boldsymbol{\mathcal{P}}_p - \varepsilon\boldsymbol{\mathcal{P}}_g$, to obtain

$$\partial_t \Delta\boldsymbol{\mathcal{P}} = \Delta\boldsymbol{\mathcal{A}} - (1+\varepsilon)\omega_p \Delta\boldsymbol{\mathcal{P}}. \tag{4}$$

Solving this equation for $\Delta\boldsymbol{\mathcal{P}}$ over the interval $[t,\ t+\Delta t]$ is possible assuming that $\Delta\boldsymbol{\mathcal{A}}$ is constant over the time interval. This is relevant for second-order time integration schemes, commonly found in finite-volume methods. Its value is either the one at time t for the first step of integration over $[t,\ t+\Delta\ t/2]$, or the one estimated at $t+\Delta\ t/2$ for the final step of integration over $[t,\ t+\Delta\ t]$. We can integrate over the time step as a function of a local time $t' \in [0,\ \Delta\ t]$. The general solution of Equation (4) is combined with the initial condition

that $\Delta\mathcal{P}(t'=0)=\Delta\mathcal{P}(t)$ at the beginning of the time step. As a result, we obtain

$$\Delta\mathcal{P}(t')=\frac{\Delta\mathcal{A}}{(1+\varepsilon)\omega_p}(1-\exp[-(1+\varepsilon)\omega_p t'])+\Delta\mathcal{P}(t)\exp[-(1+\varepsilon)\omega_p t'], \quad (5)$$

which is exact as long as ω_p is constant over the time interval.

There are two interesting regimes where this solution could be simplified in order to decouple the drag force operator from the advection, which may be required by some numerical schemes based on Riemann solvers. We first consider the regime when $(1+\varepsilon)\omega_p t'$ is small. In this case, the Taylor expansion of the exponential function in factor of $\Delta\mathcal{A}$ shows that the term depending on the presence of dust, i.e., in ω_p, appears at the order in t'^2. This term is neglected by the numerical scheme because the time integration scheme for advection is only second order, i.e., integrates only terms up to t'. Moreover, the expansion of the exponential in factor of $\Delta\mathcal{P}(t)$ contains terms in ω_p already at the order in t'. Then the term in $\Delta\mathcal{A}$ can be ignored and the solution can be simplified to

$$\Delta\mathcal{P}(t')=\Delta\mathcal{P}(t)\exp[-(1+\varepsilon)\omega_p t'], \quad (6)$$

which is the solution of the differential equation without the term in $\Delta\mathcal{A}$. Importantly, in this case, solving Equation (4) is possible by superposition of linear solutions. The integration of the terms depending on advection, $\mathcal{A}$, is done by the numerical scheme, as usual.

Second, we consider the regime when $(1+\varepsilon)\omega_p t'$ is large, i.e., for short friction times, high dust-to-gas ratios, or coarse resolutions ($t'\sim\Delta t$ is large). In this case, Equation (4) can be simplified according to the following argument: The operators $\mathcal{A}_g$ and $\mathcal{A}_p$ are dominated by terms in $\Omega_k\sigma V$, so that in amplitude the term $\Delta\mathcal{A}$ is comparable to $\Omega_k\Delta\mathcal{P}$. As a consequence, in the right-hand terms of Equation (4), the dominant one is $-(1+\varepsilon)\omega_p\Delta\mathcal{P}$ when $(1+\varepsilon)\,\omega_p\gg\Omega_k$. In this limit, the equation becomes

$$\partial_t\Delta\mathcal{P}=-(1+\varepsilon)\omega_p\Delta\mathcal{P}, \quad (7)$$

giving the same solution as Equation (6). This regime corresponds to the short friction-time approximation used to estimate the terminal velocity of the dust in many studies (Johansen & Klahr 2005; Booth et al. 2015; Lin & Youdin 2017).

To conclude, the drag force source term in the equations of conservation of movement can be expressed as

$$\pm\omega_p\Delta\mathcal{P}(t)\exp[-(1+\varepsilon)\omega_p t'], \quad (8)$$

over the time interval of integration, with + for the gas and − for the particle fluids. We can interpret it as a modified Epstein drag law, which takes into account the two asymptotic regimes discussed previously. The intermediate regime, $(1+\varepsilon)\omega_p t'\sim 1$, may suffer from neglecting the coupling with $\Delta\mathcal{A}$, but the deviation is small because the neglected term is at least one order smaller in time and $\Delta\mathcal{A}(t)$ becomes increasingly smaller as $(1+\varepsilon)\omega_p t'$ increases. The main advantage of this modified friction is the ability to model large and small dust grains without the need to modify the time step or the numerical scheme.

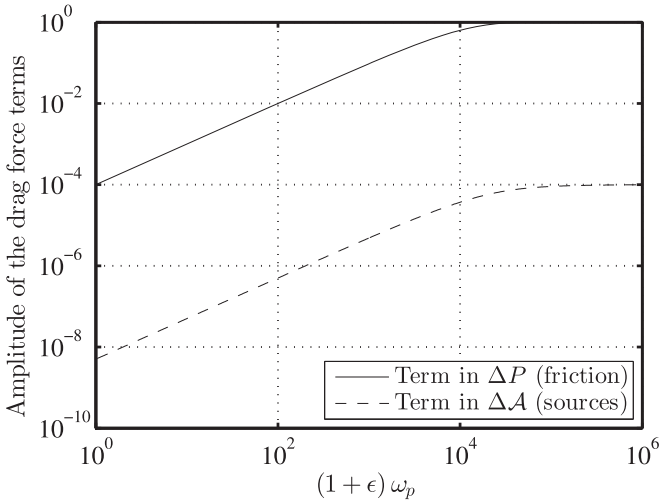

Figure 1. Estimation of the error induced by the implicit drag solution. Using a typical time step such as $\Omega_0\Delta t=10^{-4}$, we show the amplitude of the two components of the drag force integral as a function of ω_p, i.e., Ω_k/St. We observe that the term of friction in $\Delta\mathcal{P}$ (solid line) is 10^4 times larger than the contribution of the advection and source terms, $\Delta\mathcal{A}$ (dashed line).

2.2. Source Integral of the Friction

The time evolution of the momentum equations is solved by integrating the system of Equations (1) over the time step, giving for the gas

$$\mathcal{P}_g(t+\Delta t)-\mathcal{P}_g(t)=\int_t^{t+\Delta t}\mathcal{A}_g dt'+\int_0^{\Delta t}\omega_p\Delta\mathcal{P}(t)\exp[-(1+\varepsilon)\omega_p t']dt', \quad (9)$$

and for the particles

$$\mathcal{P}_p(t+\Delta t)-\mathcal{P}_p(t)=\int_t^{t+\Delta t}\mathcal{A}_p dt'-\int_0^{\Delta t}\omega_p\Delta\mathcal{P}(t)\exp[-(1+\varepsilon)\omega_p t']dt', \quad (10)$$

where $\Delta\mathcal{P}(t)=\mathcal{P}_p(t)-\varepsilon\mathcal{P}_g(t)$, and $\varepsilon=\sigma_p(t)/\sigma_g(t)$ are evaluated at time t.

The integration of the advection and source terms in $\mathcal{A}$ is made in the normal way specified by the numerical scheme that is used, while the modified friction source term is integrated analytically as follows:

$$\int_0^{\Delta t}\omega_p\Delta\mathcal{P}(t)\exp[-(1+\varepsilon)\omega_p t']dt'=\frac{\Delta\mathcal{P}(t)}{(1+\varepsilon)}\times[1-\exp[-(1+\varepsilon)\omega_p\Delta t]]. \quad (11)$$

Decoupling the friction from the full Euler equations in this manner yields a second-order accurate implicit time-stepping scheme.

Figure 1 compares the coefficients in front of each term in the exact solution of Equation (5), assuming $\Omega_0\Delta t=10^{-4}$, a typical value in the numerical setups presented in this study. The solid line corresponds to the term directly related to the drag force. The dashed line is the coefficient multiplying $\Delta\mathcal{A}(t)$ that comes out from Equation (5). In the regime of $(1+\varepsilon)\omega_p$ small (here we are limited to 1 as $St<1$ by assumption), we find that this amplitude is smaller than the one of $\Delta\mathcal{P}$ by a factor Δt, as mentioned earlier. In fact, this ratio of amplitudes is conserved up to the asymptotic case of short friction, $(1+\varepsilon)\omega_p\gg 1$. Furthermore, the value of $\Delta\mathcal{A}(t)$

converges to zero in the limit of fully coupled fluids, as the velocity difference between gas and dust will tend to zero.

As a conclusion, using a modified friction source term as proposed in Equation (8), and integrating it implicitly for t' over the time step gives an accurate approximation of the drag force because the coupling with advection and other operators is one order smaller in time. This implicit scheme given by Equation (11) for the drag force is implemented into the code RoSSBi using the following operator-splitting method:

1. Euler variables are updated from time t to $t + \Delta t/2$ with the implicit drag force,
2. advection and other sources are integrated from t to $t + \Delta t$ from the estimates of Euler variables provided by the previous step.
3. Euler variables are finally updated from $t + \Delta t/2$ to $t + \Delta t$ with the implicit drag force computed from the estimates of Euler variables provided by the previous step

This way of splitting the operators is also second order in time, so it does not degrade the accuracy of the advection scheme. This kind of semi-implicit scheme has been implemented in various methods based on particle approach (Lagrangian or SPH) for treating dust-gas interaction (Booth et al. 2015; Yang & Johansen 2016), but we propose a new implementation for multifluid methods. This updated version of the code RoSSBi is thus very efficient in following the dynamics of dusty flows for any grain size, and/or of local dust-to-gas ratios. It enabled us to investigate the evolution of a dusty vortex in presence of grains much smaller than in our previous study.

3. Numerical Simulations Setup

In this section, we present the setups of the numerical simulation runs we performed to investigate the evolution of a vortex in presence of small dust grains. We use the same context as in Surville et al. (2016) and follow the evolution of a vortex with parameters

$$(Ro,\ \chi_r,\ \chi_\theta) = (-0.13,\ 0.1,\ 6.5), \tag{12}$$

for which we have observed that the formation of a dust ring was possible for grains of $St > 4 \times 10^{-2}$.

The disk profiles are the same for all the simulations, with background gas density and temperature: $\sigma_0(r) \propto (r/r_0)^{\beta_\sigma}$ and $T_0(r) \propto (r/r_0)^{\beta_T}$. The power-law exponents are fixed to standard values, $\beta_\sigma = -1$ and $\beta_T = -0.5$. The isothermal disk scale height at the reference radius $r_0 = 7.5$ au is $H_0(r_0) = 0.05\ r_0$. The only parameter that differs from Surville et al. (2016) is the density slope, which was $\beta_\sigma = -1.5$. We chose to use a shallower power-law index for the surface density in this study in order to slow the migration speed of the vortices through the disk. According to the dust capture model developed in Surville et al. (2016), the capture timescale of the dust, $\tau_{1/2}$, scales as St^{-1}. So we follow the vortex evolution typically over several thousand disk rotations. The observed migration of the vortex must be slow enough to keep it inside the disk domain over this period.

The dust population is initially distributed with a density of $\epsilon\sigma_0(r)$, setting the initial dust-to-gas ratio to $\epsilon = 10^{-2}$. This value is the same for all the simulations; only the grain size r_s varies in this study to explore different Stokes numbers.

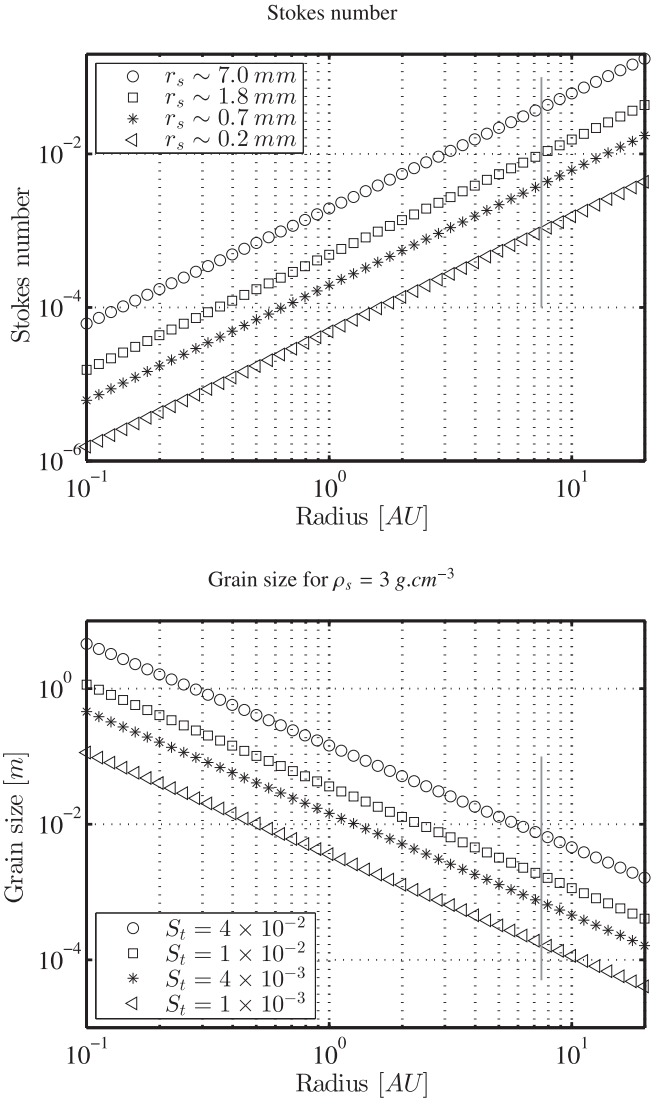

Figure 2. Top: variations of the Stokes number in the disk for different grain sizes (symbols). Bottom: variations of the grain size in the disk for different Stokes numbers (symbols). For both plots, we compute the values based on Equation (13) and assuming the disk model we used in the simulations that is described in Section 3. The vertical gray line identifies the reference radius we used in our simulations.

Recalling that the Stokes number equals

$$St = \frac{\pi}{2}\rho_s r_s \sigma_g^{-1}, \tag{13}$$

using an internal grain density of $\rho_s = 3\ \mathrm{g\ cm^{-3}}$, we can relate the Stokes number at the reference radius r_0 to a grain size. To this end, we use the gas surface density normalization, which is $\sigma_0(r_0) = 83\ \mathrm{g\ cm^{-2}}$ in this study. We consider four different Stokes numbers in this paper, $St = [1, 4, 10, 40] \times 10^{-3}$, which is almost two orders of magnitude smaller than the values used in Surville et al. (2016) and other studies.

As shown in Equation (13), the relation between the Stokes number and the grain size also depends on the location in the disk through the local gas surface density σ_g. This dependence is presented Figure 2 for the disk profile used in this study, which is similar to the MMSN model. First, the top panel shows that for a given grain population of radius r_s, the corresponding Stokes number increases with distance from the

central star. Thus, grains orbiting at 1 au will experience Stokes numbers ∼50 times smaller than similarly sized grains orbiting at the reference radius of $r_0 = 7.5$ au. Even a centimeter-sized population will have a Stokes number smaller than 10^{-2} (the commonly used value in numerical studies) in the disk region from 0.1 to 2 au, which promotes the necessity to precisely resolve the drag interaction in the regime of small Stokes numbers.

Second, the bottom panel shows which grain sizes correspond to the Stokes numbers we used in this study as a function of the orbital distance. It is striking that even a Stokes number as small as 4×10^{-3} (asterisk) would represent the dynamics of grains of a few centimeters (so-called pebbles) at 1 au. We recall that centimeter-sized grains are critical in the pebble accretion scenario, which is argued to be an efficient way to grow the rocky cores of massive planets such as gas giants (Chatterjee & Tan 2014; Lambrechts et al. 2014; Levison et al. 2015). The Euler equations being invariant as a function of the gas density normalization (as long as the disk gravity is neglected), the results presented in this study could be applied at different positions in the disk, with respect to the scalings shown in these plots. We thus give insight to the dynamics of different grain sizes in different regions of the disk.

We performed global 2D simulations with the code RoSSBi (Surville et al. 2016), which is now updated with the scheme presented Section 2 to handle the small Stokes number regime. We tested our implementation of the new implicit algorithm in this paper against a previous case run performed in Surville et al. (2016) with $St = 4 \times 10^{-2}$. The results matched to within the numerical noise level of the simulation, showing that the new implementation of the friction is robust even for noncritical Stokes numbers. After performing convergence tests with resolutions of $(N_r, N_\theta) = (2048, 4096)$, we concluded that a resolution of $(N_r, N_\theta) = (1024, 2048)$ is enough to resolve the dynamics of the systems we consider. One run with $St = 4 \times 10^{-3}$ was performed with twice the resolution in order to follow the evolution of the dusty vortex in greater detail.

4. Results of the Simulations

4.1. Results of the Main Runs

We report and describe here the results of the four main simulations, investigating the evolution of vortices in the presence of dust populations with Stokes numbers $St = [1, 4, 10, 40] \times 10^{-3}$. We cover a range of values larger than an order of magnitude. In order to present the time evolution of the disk in a concise manner, we show for each run the time evolution of (i) the azimuthal minimum of the Rossby number $Ro = \| \boldsymbol{\nabla} \times [\boldsymbol{V} - \boldsymbol{V}_0(r)] \| / [2\Omega_k(r)]$, with $\boldsymbol{V}_0(r)$ the disk background velocity, and (ii) the azimuthal maximum of the normalized dust density $\sigma_p / [\epsilon \sigma_0(r)]$. These extrema highlight the concentrations obtained in the vortex, and allow us to present in Figure 3 the whole evolution of the four runs.

A case with $St = 4 \times 10^{-2}$ and $\epsilon = 10^{-2}$ was presented in Surville et al. (2016), but was only followed for 500 disk rotations. In this study, we evolve the case with $St = 4 \times 10^{-2}$ (first row) during 1200 disk rotations until we observe a significant numerical dissipation of the structures. We observe three phases of evolution, in agreement with the results of Surville et al. (2016). First, a phase of dust capture into the vortex occurs during the first hundred disk rotations, which can be seen in the dust density map (right) as a conic shape, revealing the inflow of dust toward the vortex center. Then the vortex instability develops at $t = 100$ rotations, generating some strong vorticity throughout the vortex and further increasing the maximum dust density. The regime of the unstable dusty vortex continues for almost 200 rotations, until time $t = 380$ rotations. During this period, dusty eddies are generated and destroyed inside the vortex, but never reorganize into a smooth structure. As a result, the dust density has a radially extended maximum, covering the majority of the vortex surface, as opposed to the strong confinement in the vortex center observed prior to the onset of the instability. Finally, the vortex is stretched along the whole azimuthal direction, and a turbulent dust ring forms. It consists of several dusty eddies and filaments evolving at different orbits, which explains the wide radial extent of the dust density maximum, which is almost $0.1 r_0$. After $t = 800$ disk rotations, the numerical diffusion dissipates the eddies into a quasi-axisymmetric, quiet dust ring. In this near steady state, the maximum dust density drops to around 50 times the dust background.

When we reduce the Stokes number to $St = 10^{-2}$ (second row), we obtain a similar sequence of events. The dust capture into the vortex occurs on a longer timescale, approximately 300 disk rotations, before the vortex instability develops. Surville et al. (2016) derived an analytical formulation of the capture time, $\tau_{1/2}$, which was approximately proportional to $1/St$ for the well-coupled grain regime, explaining a longer period of capture. Compared to the previous case, the Stokes number is reduced by a factor of 4, but the time of the end of the capture is only longer by a factor of 3. We explain this discrepancy in the next section. After the vortex instability, the disk enters a long phase when the unstable dusty vortex survives and resists destruction. Similarly to the case with $St = 4 \times 10^{-2}$, the structure remains turbulent, and the vortex splinters and eventually dissolves. This period lasts for almost 900 disk rotations, until $t = 1200$ rotations. After this time, the disk enters the dust ring phase, which lasts 500 rotations, with robust dust eddies and filaments surviving. In particular, two persistent small dusty vortices detach from the main region of formation, and can be seen in the plots after $t = 1200$ rotations in the region $0.8 < r < 0.9 r_0$. After $t = 2200$ disk rotations, the structures are dissipated by the numerical diffusion.

In the third row, we present the results obtained with $St = 4 \times 10^{-3}$. In this case, the capture of dust into the vortex takes about 700 disk rotations before the vortex becomes unstable. However, a significant difference with the previous cases is visible. Just after the instability, the vortex again becomes quiet between approximately $t = 700$ and $t = 1000$ rotations. The dust density map shows (on the right) that a capture is again at work, revealed by the characteristic conic shape. A series of three additional vortex instabilities occurs during the period between $t = 700$ and $t = 1700$ disk rotations. This new phase of evolution of the dusty vortex is visible only for small well-coupled grains and is discussed in the next section. After this phase, the vortex is unstable, and persists in the disk until $t = 2800$ rotations, with a high dust loading. Inside the vortex, the dust density is enhanced by more than 500 times, and the local dust-to-gas ratio is in the range 5–8. Finally, the dusty vortex is destroyed and a dust ring forms and evolves during the last 500 rotations of the simulation. We could not follow the evolution much longer, but based on the

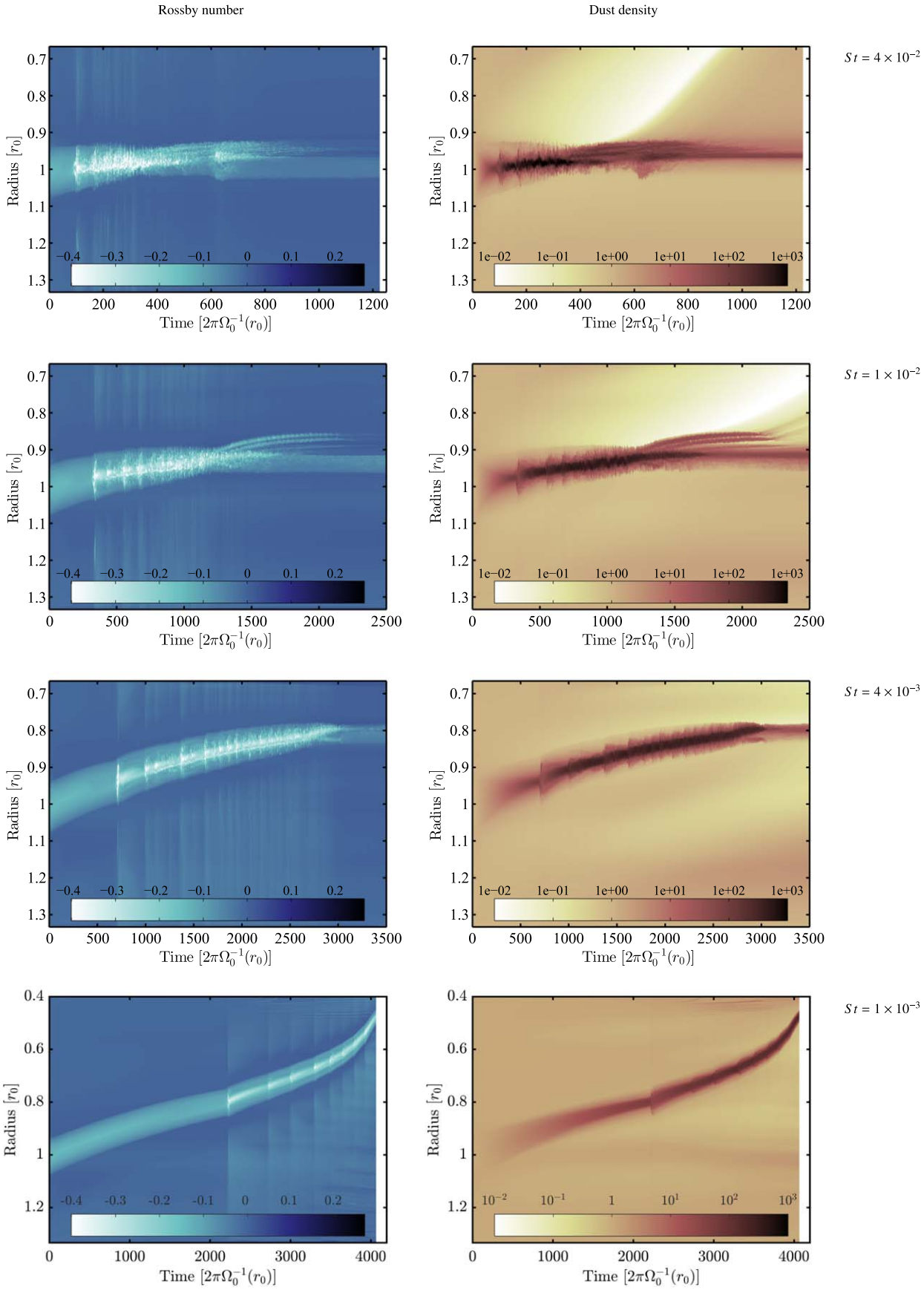

Figure 3. Results of the main runs. Long-term evolution of the azimuthal minimum of the Rossby number (left), and of the maximum of the dust density (right) for different values of the Stokes number. From top to bottom: $St = 4 \times 10^{-2}$, $St = 1 \times 10^{-2}$, $St = 4 \times 10^{-3}$, and $St = 1 \times 10^{-3}$, respectively. The dust density is relative to the background disk.

dissipation observed during the last hundred orbits, the dust ring may persist for a long time after the end of the run.

The last setup of the main runs (bottom row) is performed with $St = 10^{-3}$. The disk domain is more extended, with $0.4 < r < 1.5r_0$ to provide even more room for radial migration. In order to keep a comparable numerical resolution with the other runs, we used $(N_r, N_\theta) = (2048, 2048)$ grid cells. Assuming a grain density in the range of $\rho_s = 1$–$3\ \mathrm{g\,cm^{-3}}$, the grain size corresponding to this Stokes number range is $r_s = 0.2$–0.5 mm. Such small dust grains are well coupled and are expected to have a negligible deviation from the gas streamlines. However, this small discrepancy is still enough to cause the dust to deviate from the gas motion if the evolution is followed for a sufficiently long time. Our results show that even for such a small Stokes number, the capture of the solids into the vortex is efficient.

The dust is strongly accumulated to a critical density of 50 times the background, and the vortex instability develops at $t = 2100$ disk rotations. A second period of dust capture follows, from $t = 2100$ to $t = 2800$ disk rotations, and ends in a second event of vortex instability. This process again occurs three times until $t = 3600$ disk rotations, and is responsible for a significant increase in dust density inside the vortex. After this phase, the vortex suffers an unstable evolution, as observed in the other runs, but its high vorticity quickly fastens its radial migration. Even with this extended disk run, the vortex is not destroyed after 4000 disk orbits of evolution, and we stop the simulation before we observe the formation of a dust ring. However, at the end of the run, the vortex is very turbulent and is much more elongated than at an earlier stage of evolution. This is evidence of destabilization and possible vortex destruction, but this conclusion is not fully confirmed by the numerical simulation.

Vortex migration is particularly visible in the $St = 4 \times 10^{-3}$, and $St = 1 \times 10^{-3}$ runs. Even if the axes of the figures are different due to different disk size, in the two runs the vortex migration rate of $-1 \times 10^{-4} r_0$ per disk rotation is similar. It is not affected by the grain size; indeed, it depends mostly on the local disk conditions and on the vorticity of the vortex (Paardekooper et al. 2010; Surville & Barge 2012, 2013). In fact, migration of the vortex occurs in the four runs, but the vortex is destabilized for the larger grains before it can migrate very far. For the smaller grains, because the capture timescale is much longer, the migration of the vortex is more apparent. In fact, for the $St = 1 \times 10^{-3}$ case, the vortex even reached the inner boundary before it is destroyed into a dust ring.

4.2. Results of the High-resolution Run

The high-resolution run is devoted to study the evolution of the dust ring obtained in the $St = 4 \times 10^{-3}$ case with higher accuracy. The first motivation is that dust rings are composed of small-scale eddies and filaments, which require high resolution to be well resolved. The second motivation is that using a resolution of $(N_r, N_\theta) = (2048, 4096)$, we can compare this additional run with the results of Surville et al. (2016), who used larger Stokes numbers. We have anticipated the possible radial migration of the vortex that was observed in the main run, and used a disk inner boundary at $r = 0.6r_0$ rather than $2/3$. All the other parameters are the same as in the main run (except for the resolution). The analysis of the high-resolution additional run is presented Figure 4.

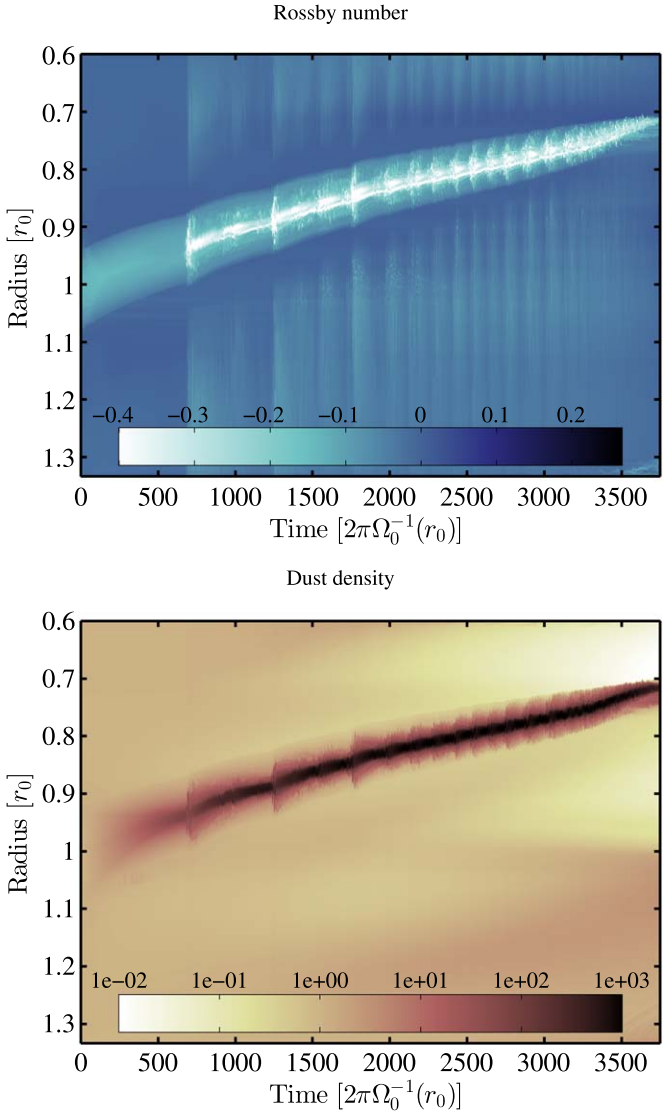

Figure 4. High-resolution run for $St = 4 \times 10^{-3}$, using a numerical resolution of $(N_r, N_\theta) = (2048, 4096)$. We show the long-term evolution of the azimuthal minimum of the Rossby number (top), and of the maximum of the dust density (bottom).

The evolution begins with the dust capture, the duration of which is almost identical to the results of the main run. The effect of the resolution is minor during this phase, implying that the main runs have enough resolution to capture the process accurately. The vortex instability develops at $t = 700$ disk rotations and is followed by a second phase of capture. However, this second phase is almost twice as long as in the main run, and the dust is more confined inside the vortex. A second event of instability starts at $t = 1250$ disk rotations and results in a vortex with a turbulent core, the size of which is significantly wider than after the first event of instability. Then the vortex calms down, and dust is again accumulated in its core. At $t = 1700$ rotations, another vortex instability occurs, followed by a short period of dust capture. After these three main instability events, which affect the vortex from its center to its border, the vortex cannot calm down or resist the turbulent flow sustained in its core. Over $\sim$2000 disk rotations, the nonlinear state of the two-fluid instability saturates, and a frequent repetition of weaker instabilities at the vortex core is observed. The distinction between the different phases is more

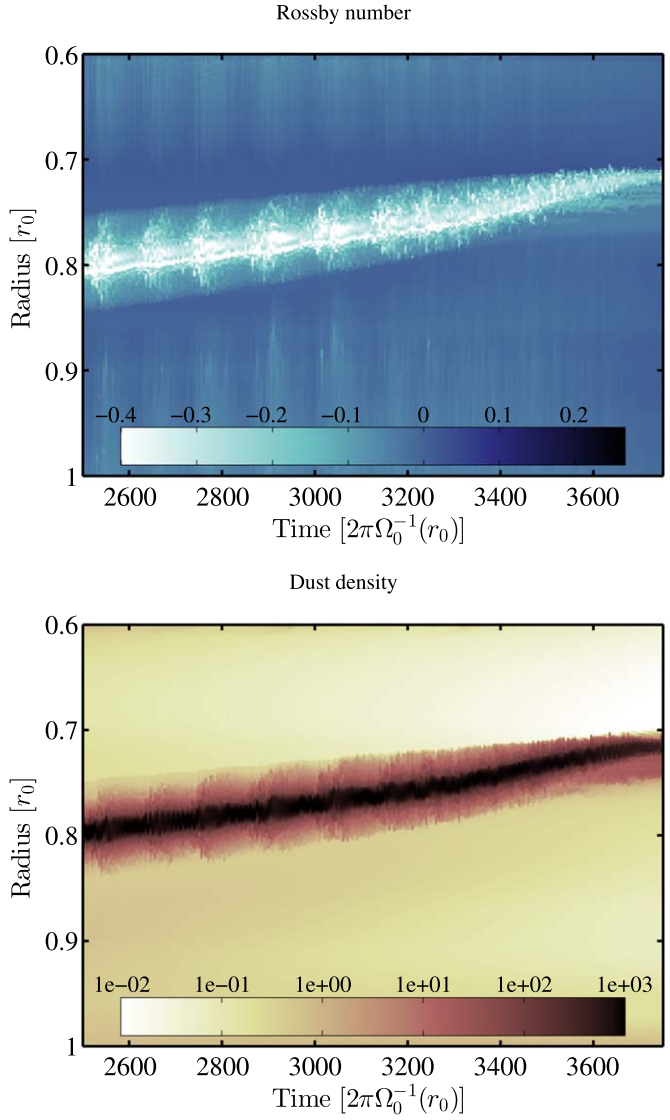

Figure 5. Ring-formation phase for the high-resolution run. We show the same results as in Figure 4, but we focus on the last thousand orbits and have zoomed in radially.

evident in the high-resolution results than in the main run. The vortex migration is also more prominent in the high-resolution run, probably because the vortex flow has less numerical dissipation.

The formation of a dust ring was observed in the high-resolution run at $t = 3400$ disk rotations. It is significantly later than in the main run ($t = 2800$ rot.) because the phase of sustained turbulence lasts longer in this additional run. Figure 5 zooms in on the last thousand disk rotations of the simulation, when dust ring formation occurs. After $t = 3400$ rotations, the vortex suffers destruction and dusty eddies are spread in the disk. This is visible in the Rossby number plot as horizontal stripes created at $0.70 < r < 0.75 r_0$. The dust density enhancement is kept higher than 50 times in this region, in particular in a narrow region close to $r = 0.71 r_0$, where it is almost 10^3 higher than the disk background.

In this section we have described the numerical results obtained for different grain sizes in the context of interaction with a large-scale vortex. In summary, we observe the same phases of vortex evolution at smaller grain sizes that we observed previously in Surville et al. (2016), i.e., the initial capture of dust, the vortex instability, the unstable evolution when an active dusty flow is sustained inside the vortex, and the eventual dust ring formation. However, the duration of capture in the vortex is shorter for larger grains, and the repetition of instabilities of the vortex was discovered only for small grains, i.e., $St < 4 \times 10^{-3}$.

5. Discussion

This section is devoted to provide more insights into the different processes described in the previous section, and we discuss the consequences for planet formation scenarios.

5.1. Dust Distribution during Capture

In all the simulations performed with different grain sizes, the capture of solids inside the vortex was observed in the first phase of evolution. As discussed in the previous section, the estimated timescale of capture shows that it takes longer for smaller grains to accumulate to the critical point where the vortex is destabilized. This result was discovered in Surville et al. (2016) for $0.04 < St < 0.36$, and is extended to $St = 10^{-3}$ in this study. We compare here the capture observed in the simulations with the analytical model to infer the robustness of the model and to confirm the physics behind this capture.

The analytical model of linear capture developed in Surville et al. (2016) is based on the coupled evolution of the gas and dust fluids. We do not detail the calculation here, but refer to Section 3 of this reference, but we recall the main equations of the coupled system:

$$\begin{aligned} \partial_T \sigma_p^* &= 4\pi A |Ro| \sigma_p^*, \\ \partial_T |Ro| &= -4\pi A \tilde{\epsilon} |Ro| \sigma_p^*. \end{aligned} \tag{14}$$

Here σ_p^* is the maximum of the dust density at the vortex center normalized to $\epsilon\sigma_0(r)$, $|Ro|$ is the absolute value of the Rossby number, $T = 2\pi\Omega_0^{-1}$ is the local period at the vortex orbit, and $\tilde{\epsilon} = (1 + \beta_\Omega/2)\,\epsilon\sigma_0(r)/\sigma_g$ is a modified dust-to-gas ratio at the vortex center. The parameter $A = 2St/(1 + St^2)$ represents the degree of coupling between the two fluids.

From this coupled system of equations, we can compute the time evolution of $\sigma_p^*(T)$ as

$$\sigma_p^*(T) = 1 + |Ro|\tilde{\epsilon}^{-1} \times \frac{1 - \exp(-4\pi A I_0 T)}{1 + |Ro|\tilde{\epsilon}^{-1}\exp(-4\pi A I_0 T)}, \tag{15}$$

with $I_0 = \tilde{\epsilon} + |Ro|$ estimated at the beginning of the simulation, i.e., at $t = 0$.

The main difference between the cases of well-coupled grains and larger grains relies on a significant vortex migration. This effect is due to the long duration of the capture before the vortex becomes unstable. Thus the local orbital period of the vortex T in the model may change as long as the dust is accumulated. However, this change is slow, and can be estimated as $T(r_v) = 2\pi\Omega_0^{-1}(r_v)$ with the vortex orbit $r_v = r_v|_{t=0} + v_{\rm mig} T$. The measured migration velocity of this vortex is $v_{\rm mig} = -1 \times 10^{-4}\, r_0/T(r_0)$. In practice, we have measured the orbit of the vortex as a function of time for the different runs, and used these values for r_v. The change of $T(r_v)$ being slow, the integration of the system (14) with a varying T can be approximated to a good accuracy by only replacing T by $T(r_v)$ in the solution for Equation (15).

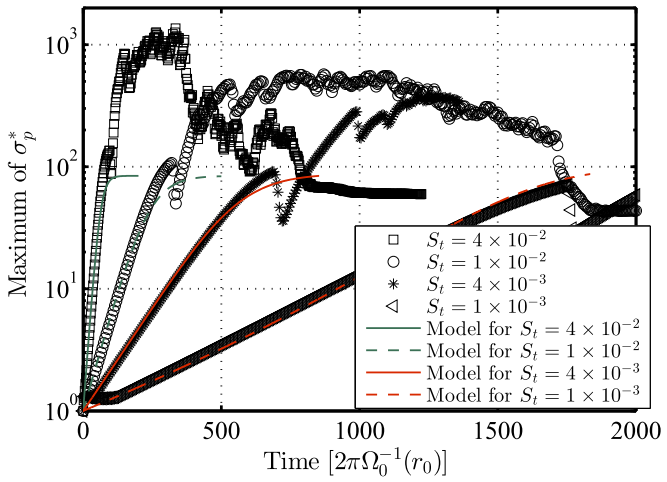

Figure 6. Linear dust capture into the vortex. We show the evolution of the dust maximum density relative to the disk background for different grain sizes (symbols). The lines represent the evolution predicted from the dust capture model of Surville et al. (2016). A very good agreement is obtained when the vortex migration is taken into account, which modifies the local time reference (because $\Omega_k(r)$ becomes smaller with r).

The comparison of this modified model with the main runs is presented Figure 6. The symbols represent the four different Stokes numbers we used in the main runs. The result of the model is plotted for each number with a colored line. It is striking that the increase of the maximum of dust density at the vortex center follows an exponential growth as predicted, even for Stokes numbers as small as 10^{-3}. The growth rates of the maximum dust density are correctly estimated by the modified model for all the tested grain sizes, which confirms its validity for a wide range of grain sizes and vortex profiles.

We can be confident that the drag interaction between gas and dust is responsible for the accumulation of solids in anticyclonic regions, as described by our model. The correction of the local orbital period, necessary to fit the numerical results, has significant implications. It shows that the exponential growth of the dust density depends on local conditions of the dusty vortex, and on the grain size. We show evidence that there is no critical grain size (or Stokes number) for which this growth disappears. In fact, even well-coupled dust grains undergo the capture due to the drag. As predicted by our capture model, the growth rate asymptotically tends to zero as the Stokes number decreases because of the proportionality in this regime.

Despite this analytical result, there must in reality be a threshold in Stokes number below which this capture would be too long to be relevant. Considering for example that at a few au, the giant planet cores are formed by core accretion within several million years, the planetesimal formation must occur on faster timescales. As a consequence, the solid material contained in small dust grains must assemble even faster into pebbles and planetesimals. This implies an upper limit on the timescale in which this scenario of capture and subsequent collapse of high concentrations of small grains is useful. When we estimate the capture timescale from the results of the analytical model of Surville et al. (2016; see Equation (38) of this reference), and limit it to 10^5 orbits at 5 au, we find a minimum Stokes number in the range 10^{-5}–10^{-4}. There is one final limiting factor: the survival of large-scale vortices over such a long period. One can reasonably reduce this estimate by a factor of ten and argue that grains of Stokes numbers smaller than 10^{-4} cannot contribute to the disk evolution in the scenario of vortex-driven planetesimal formation.

It is also important that we consider the duration of capture. The analytical model predicts that the maximum density of dust achieved at the end of capture is the same for all the Stokes numbers because this value only depends on the Rossby number of the vortex and on the initial dust-to-gas ratio. This is confirmed by the numerical results because we measure a dust density enhancement in the range 80–120 for the four grain sizes before the vortex instability. The analytical model of capture predicts a maximum dust enhancement of

$$\sigma_p^*(T \to \infty) = 1 + \frac{|Ro|}{\tilde{\epsilon}} \sim 85, \tag{16}$$

using the parameters of the vortex. The agreement is thus satisfying over decades of grain sizes, even when the vortex migration is significant.

The findings above suggest that the evolution of dusty vortices is self-similar during the phase of capture. Comparing a snapshot of the structure of the disk for different grain sizes requires that it corresponds to the same time during the process of capture. Defining this time correspondence is possible for example by choosing a value of dust enhancement. Here, if we choose $\sigma_p^* = 50$, the correct times for the equivalent state of evolution are $t = 61$, 235, 545, and 1540 disk rotations for $St = 4 \times 10^{-2}$, 10^{-2}, 4×10^{-3}, and 10^{-3}, respectively.

In Figure 7 we show the color maps of the Rossby number and of the dust density for the four main runs at these "equivalent" evolution times. It is striking to see how similar the distributions of dust are inside the vortex, but also the similarity of the vorticity profiles. Only the case with $St = 4 \times 10^{-2}$ shows noticeable differences, with some structures spiraling inside the vortex. Indeed, the vortex is still relaxing from the initial conditions and capturing the dust at the same time. These spirals are also visible in a run with only gas, and so not due to the presence of dust.

When we compare these snapshots, it is very difficult to distinguish between the different grain sizes. The dust grain distribution inside the vortex approximately follows the same streamlines as the gas. However, as a function of the distance from the vortex center, the density of dust is the same regardless of the Stokes number.

Our results differ from those in some recent papers that showed that the dust density profile inside a vortex depends on the grain size (Lyra & Lin 2013; Barge et al. 2017; Sierra et al. 2017). The analytical models behind these studies assume a turbulent diffusion of dust due to an unresolved (3D) turbulence, which allows for a steady state inside the vortex. This vortex turbulence may be produced by the saturation of the elliptical instability acting in incompressible vortices (Lesur & Papaloizou 2009). Thus, these studies were made for a particular category of vortices. As a result, the dependence on the grain size is effective when the accumulation of dust in the vortex is large.

In our study, the compressible vortex has open streamlines and is unaffected by this instability (similarly to the 3D vortices found in Meheut et al. 2010). This class of vortices evolves differently because the dust diffusion rises from the instability of the vortex that is triggered by the two-fluid interaction at the end of the capture phase.

The comparison between these two classes of vortices suggests that if additional turbulence exists, the changes in gas

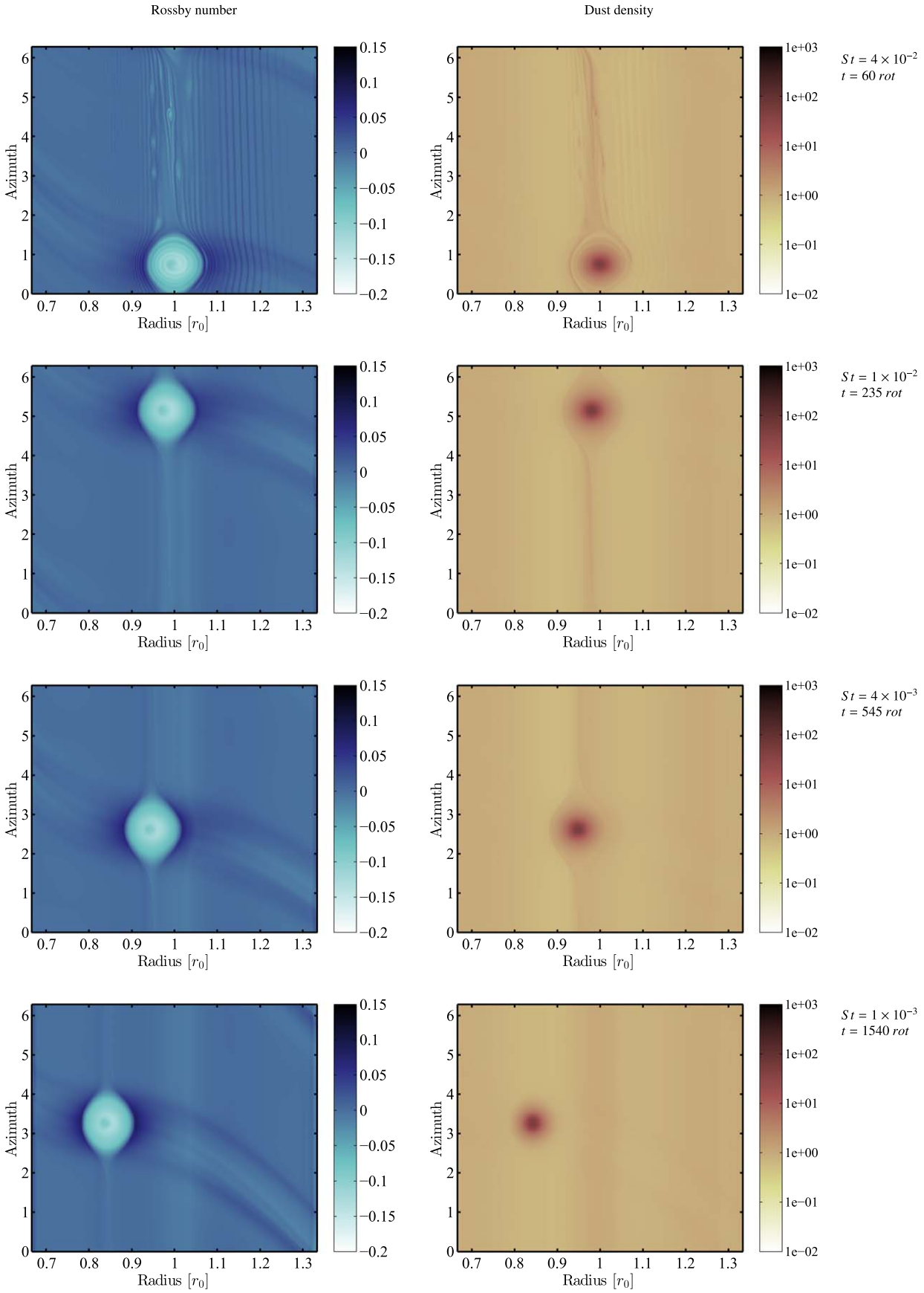

Figure 7. Disk profiles at equivalent stages of evolution in the capture phase, when $\sigma_p^* = 50$ at the vortex center. From top to bottom: Snapshots at $t = 61$, 235, 545, and 1540 disk rotations for $St = 4 \times 10^{-2}$, 10^{-2}, 4×10^{-3}, and 10^{-3}, respectively. We report the (r, θ) maps of the Rossby number on the left, and we show the maps of the dust density in a logarithmic color scale on the right.

vorticity and other profiles inside the vortex core—due to turbulence—will occur on short timescales, probably shorter than the time it takes for the drag to act on the dust. Then, the time averages over the drag timescale will be the quantities that describe the capture. We can reasonably assume that turbulence may not drastically change the capture law. Moreover, in both approaches, the concentration of solids in the vortex should be slower for smaller gains, and saturate either due to artificial diffusion or due to the two-fluid instability.

The timescale of capture is thus fundamental for comparing the evolution of different grain sizes. For example, the numerical simulations reported in Barge et al. (2017) and Sierra et al. (2017) compared the dust distribution inside a vortex for different grain sizes. This comparison was made only after 100 disk rotations, which biases the results. The smallest grains do not have time to concentrate enough to reach steady state or the vortex instability, while the largest grains will pass beyond the vortex instability. In contrast, our results suggest that the vortex evolution during the phase of accumulation is the same for all grain sizes—just with a different timescale—until saturation is reached either because of the change of the vorticity profile in our model of compressible vortices, or by the effect of turbulent diffusion in incompressible turbulent vortices.

Finally, additional processes such as considering a wide distribution of grain sizes in the disk and the possibility for grains to grow or fragment may change the density profiles in the vortex. The observability of the well-coupled grains in vortices can be explored by producing simulated images, for example of what would be seen by ALMA. The multi-wavelength maps of the vortex region could help to disentangle the grain size of the dust (Gonzalez et al. 2012). This extension of our study to the observability will be addressed in a future publication.

5.2. Effects of the Grain Size on the Vortex Instability

In all the simulations that were made with different grain sizes, from $St = 0.35$ to $St = 0.04$ in our previous study, Surville et al. (2016), and here from $St = 4 \times 10^{-2}$ to $St = 10^{-3}$, the vortex becomes unstable after the period of dust capture. The duration of the instability is very limited, it is about 50 disk rotations. Its dependence on the Stokes number of the dust fluid is difficult to estimate, and varying St over two orders of magnitude has no significant influence on the duration of the vortex instability. This observation indicates that the conditions of the flow triggering the instability are very similar in the different cases, and are likely linked to the gas profile in the vortex at the end of the process of dust capture. The similarities of the flow profiles for different grain sizes when compared at equivalent times of evolution, as discussed in the previous section (see Figure 7), corroborate this argument.

We compared the vorticity profiles of the main runs at the time when the instability of the vortex starts. These times were chosen to correspond to the equivalent states of evolution for the different grain sizes, $t = 84$, 310, 685, and 1740 disk rotations for $St = 4 \times 10^{-2}$, 10^{-2}, 4×10^{-3}, and 10^{-3}, respectively. The profiles of the Rossby numbers are shown Figure 8 and are focused on the vortex region.

To first order, the vorticity profiles look similar, with a near constant vorticity throughout the vortex ($Ro = -0.13$), and a core of nearly zero vorticity. This region surrounding the core exhibits spiral structures, which reveal the development of the vortex instability. Upon closer inspection, we see that the modal structure varies with the Stokes number of the dust. For the two largest grains, the mode structure is similar, with a mixture of modes $m = 2$ and $m = 3$ in a local frame centered on the vortex center. As pointed out previously, the spirals visible in the $St = 4 \times 10^{-2}$ case over the whole vortex are due to the vortex relaxation, and not to the interaction with dust. Thus, even if the grain size is reduced by a factor four between these two runs, the vortex profiles are surprisingly similar.

The effect of the dust Stokes number is more evident for the two smaller grains (bottom row). In the case with $St = 4 \times 10^{-3}$, the flow close to the vortex center contains a mixture of $m = 3$ and $m = 4$ modes, which is nevertheless not an impressive discrepancy with the largest grains runs with regard to the magnitude of the Stokes numbers. The last case with $St = 10^{-3}$ has the highest modes, $m = 4$ and $m = 5$; the Rossby number is also different at the vortex center: it differs from zero. The results published in Surville et al. (2016), obtained with the same vortex model and with $St = 0.17$, also exhibit the appearance of modes $m = 3$ and $m = 4$ modes at the beginning of the vortex instability (see Figure 14 of this reference).

As a consequence, varying the Stokes number from $St = 0.17$ down to $St = 10^{-3}$, i.e., over two orders of magnitude, does not modify the modal structure of the vortex instability or the growth rates because the duration of the instability is qualitatively similar. The vortex instability has no significant dependence on the Stokes number. As a last remark, we mention that the study of a dusty Rossby wave instability in Surville et al. (2016) revealed that the azimuthal modes $m = 3$, 4, and 5 were the most unstable with comparable growth rates (see Figure 16 of this reference), with $St = 0.1$. The fact that similar modes grow inside the vortex during the instability reflects the nature of the instability. It is due to the shear created in the gas by the drag back-reaction, and it drags the dust while growing.

If well-coupled grains are able to trigger the vortex instability after the exponential dust capture phase in a similar way as larger grains, the development of the instability may be sensitive to the numerical resolution. In fact, if this instability is related to the gas profile of vorticity, the typical length scale must be resolved by the numerical scheme. We explore this convergence problem by comparing the same case with $St = 4 \times 10^{-3}$ at $(N_r, N_\theta) = (1024, 2048)$ (main run) and at $(N_r, N_\theta) = (2048, 4096)$ (high-resolution run). The maps of the Rossby number of these two cases at a similar time of evolution are presented Figure 9. The snapshots are chosen in both cases when the first established modes of instability are visible inside the vortex, and a later state (five disk orbits after) show the saturation of the modes.

Whereas the medium-resolution result (main run, left panels) exhibits a mixture of modes $m = 3$ and $m = 4$ inside the vortex, the high-resolution result (additional run, right panels) shows a higher mode structure, $m = 4$–5. Even if the change is by only one mode number, it is a significant discrepancy and suggests that higher resolutions are required to obtain the full convergence of the process. However, the evolution over five orbits (bottom row) shows that the two resolutions finally evolve in a similar manner. At this stage, it is difficult to distinguish the difference of the mode numbers.

It was not possible to conduct all the cases performed in this study at such a high resolution because of the duration

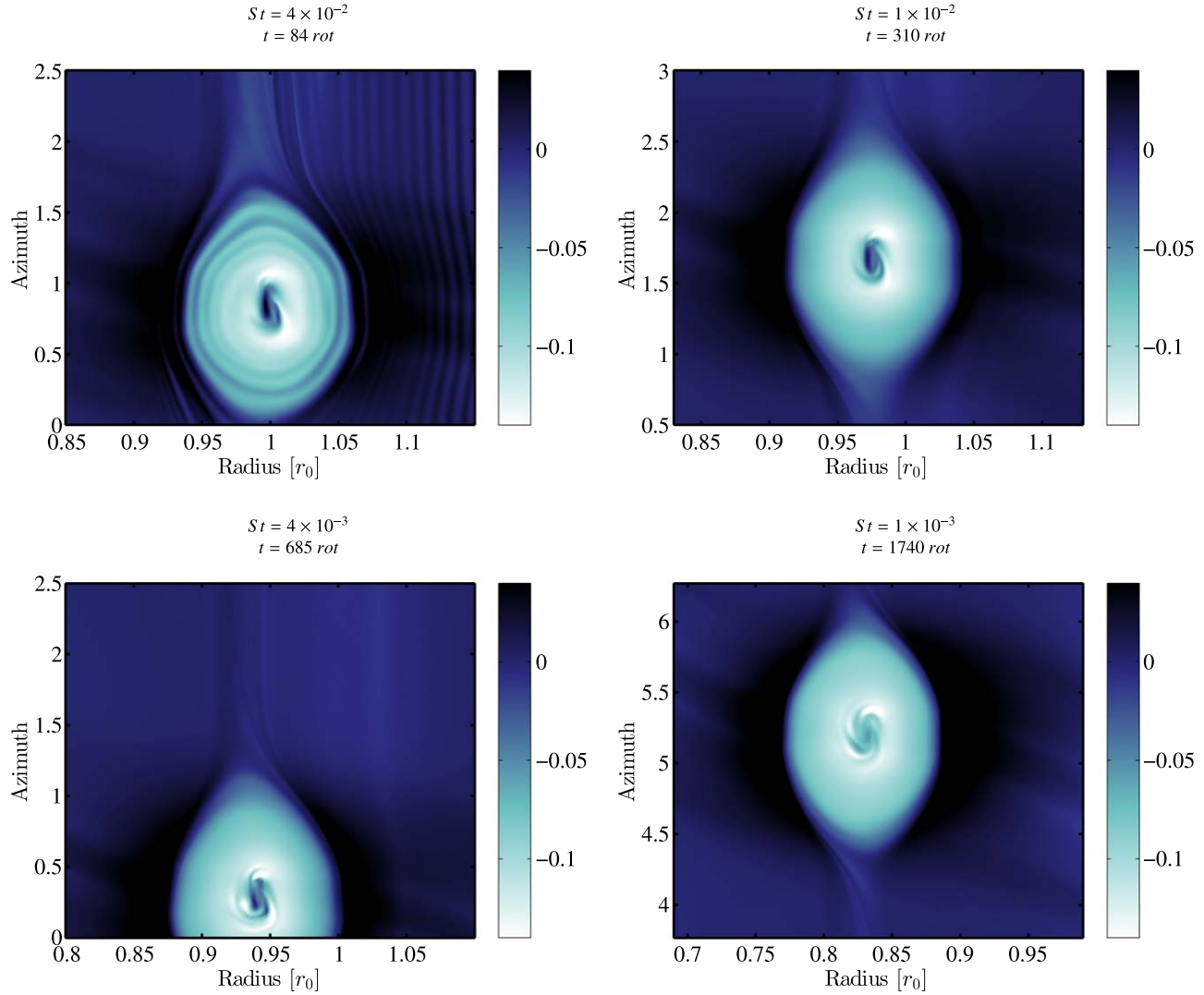

Figure 8. Saturation of the first modes during the vortex instability. We show a zoom-in of the Rossby number maps for different Stokes numbers at the time when the first most recognizable modes are established. When the Stokes number is decreased (from left to right and top to bottom), higher modes saturate: $m \sim 2$, $m \sim 2$–3, $m \sim 3$–4 and $m \sim 4$–5 for the main runs with $St = 4 \times 10^{-2}$, $St = 1 \times 10^{-2}$, $St = 4 \times 10^{-3}$, and $St = 1 \times 10^{-3}$, respectively.

necessary to cover the full evolution of the dusty vortex, i.e., up to 4200 disk rotations. The degree of convergence obtained for the main runs is nevertheless satisfactory and sufficient to provide trustful insights on the vortex instability and on the full process of evolution. Moreover, the effect of the grain size on the instability should not be affected by the used resolution, and if the growing modes could be higher than those observed in the main runs, the comparison between Stokes number values will give similar conclusions at higher resolution, i.e., the mode structure is almost not influenced by the value of *St*.

5.3. Dust Ring Evolution for Different Grain Sizes

After the capture phase and the vortex instability, which occur systematically for all Stokes numbers down to 10^{-3}, the last phase of evolution of the dusty vortex is the formation of a turbulent dusty ring. These structures were depicted in Surville et al. (2016) as a byproduct of the vortex destruction. We discuss here the particularities of these features for smaller grains and their possible implications on the formation of planetesimals.

When we described the evolution of the different runs, Section 4, we observed the formation of dust rings for the three largest Stokes numbers. The only case where the vortex survives up to the end of the simulation is with $St = 10^{-3}$. We discuss this exception in the next section. For the other dust populations, the formation of the dust ring occurs after the unstable evolution of the vortex, at a characteristic time that is longer for smaller dust grains. Figure 10 presents snapshots of the disk after 400, 1400, and 3000 disk rotations for the main runs with $St = 4 \times 10^{-2}$, 10^{-2}, and 4×10^{-3}, respectively. The choice of these times is motivated by the number of structures that are visible in the disk and in the dust rings. We also check that the vortex is fully dissipated in each case.

For the largest grains with $St = 4 \times 10^{-2}$ (first row), a chain of dusty eddies survives during a long period in the disk. The local dust-to-gas ratio is sustained to a few times unity, while smaller scale eddies and dense filaments are also present in the flow. On the left, the Rossby number map shows the large-scale turbulence of the gas in this wide dust ring. Because the effect of the drag is sufficiently fast for this Stokes number, estimated to the capture timescale i.e., around 30 rotations, new eddies form frequently following the same process as the

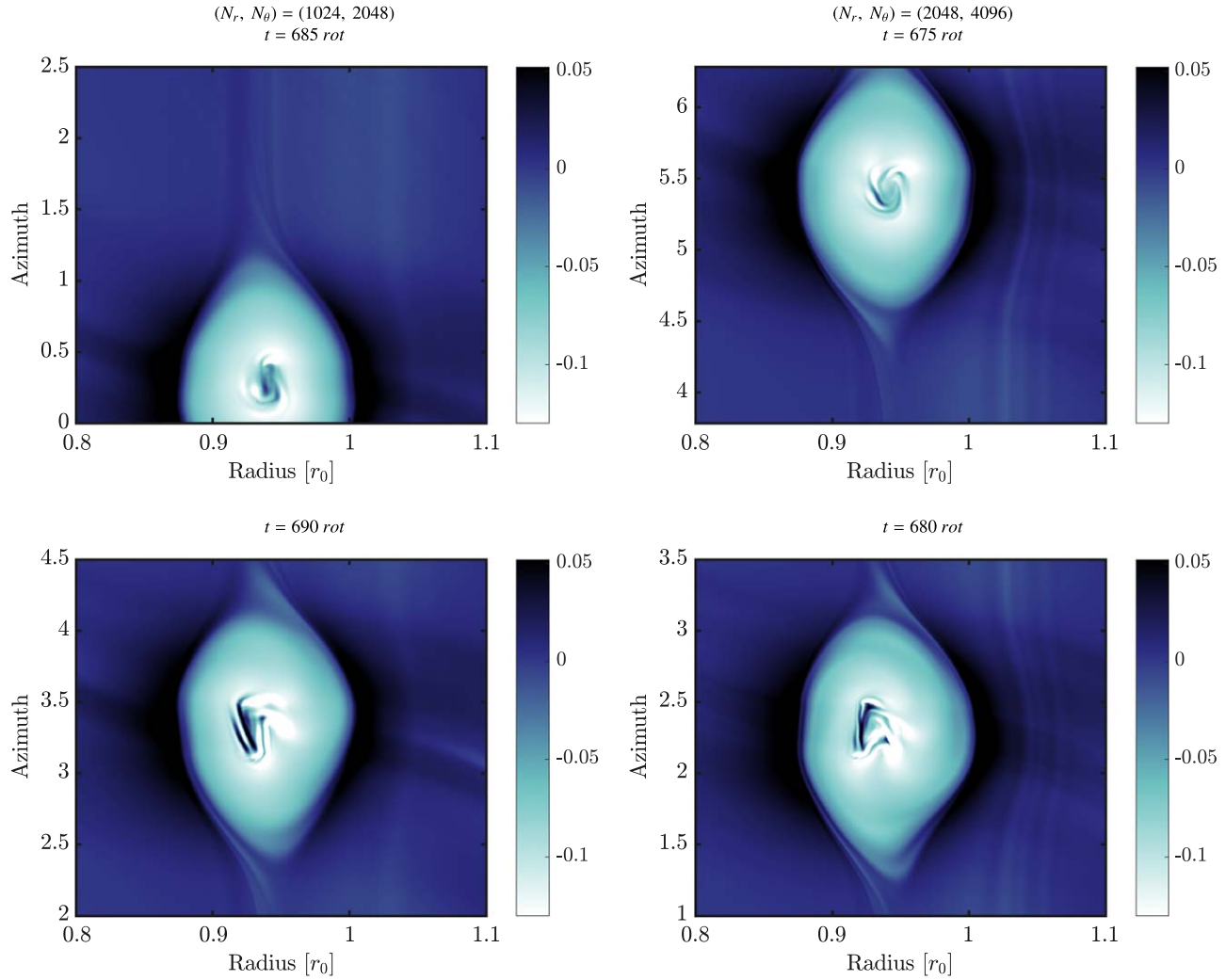

Figure 9. Effect of the resolution on the instability, with $St = 4 \times 10^{-3}$. We show a zoom-in of the Rossby number maps of the vortex when the first recognizable modes are established. Left: results of the main run, $(N_r, N_\theta) = (1024, 2048)$, at $t = 685$ rot (top) and $t = 690$ rot (bottom). The flow close to the vortex center shows a mixture of $m = 3$ and $m = 4$ modes locally, which saturate and form this typical triangular shape. Right: results of the high-resolution run, $(N_r, N_\theta) = (2048, 4096)$, at $t = 675$ rot (top) and $t = 680$ rot (bottom). The flow close to the vortex center more clearly shows a higher mode structure ($m = 4$–5), which saturates and forms this typical square shape.

vortex instability, but on smaller scales. The only source of dissipation preventing high-frequency turbulence, and eventually counteracting the drag force coupling, is numerical diffusion. In this simulation, the dust ring is sustained during approximately 500 rotations.

In the run with $St = 10^{-2}$ (second row), the dust ring forms much later, which is in agreement with the self-similarity of the dust capture with respect to the Stokes number (see Section 5.1). As the vortex had more time to migrate before it was destroyed by the instability, the dust ring is established closer to the star, in the region $0.9 < r < 0.96 r_0$. Compared to the results with larger grains, the dust eddies are less individualized and detached from the main bump of dust, where the dust-to-gas ratio is about 50%. The number of dense eddies is reduced, but the Rossby number map also reveals the presence of smaller scale turbulence (on the left). The drag force effect onto the gas, which drives this turbulent dusty flow, is acting on longer timescale in this case. As a consequence, the numerical dissipation is more prominent and counteracts the accumulation of solids in vortical regions. This accumulation is also physically slower due the the reduction of the Stokes number.

There is a clear different behavior of the evolution resulting in the dust ring formation in this case, compared to the largest grain run. Rather than forming several high-density clumps, the vortex evolution leads to only one large eddy that is a remnant of the original vortex containing material that was collected during the initial phase of dust concentration. The dust density in this clump is higher by a factor of a few than in those obtained with $St = 4 \times 10^{-2}$. Over a few hundred orbits, the highest dust-to-gas ratio in this clump is about 5.

The last case is the result with $St = 4 \times 10^{-3}$ (bottom row). The dust ring is formed much later, after ~3000 disk rotations, and it lies even closer to the inner parts of the disk. The longer evolution of the disk and of the vortex is favorable for the numerical dissipation to act. Only a few small dusty eddies remain, with a much lower density than what was seen for larger grain sizes. The turbulence and vortical substructures in the dust ring are washed out by numerical diffusion, as seen in the map of the Rossby number (left). The longer timescale of action of the drag is also not favorable for sustaining the

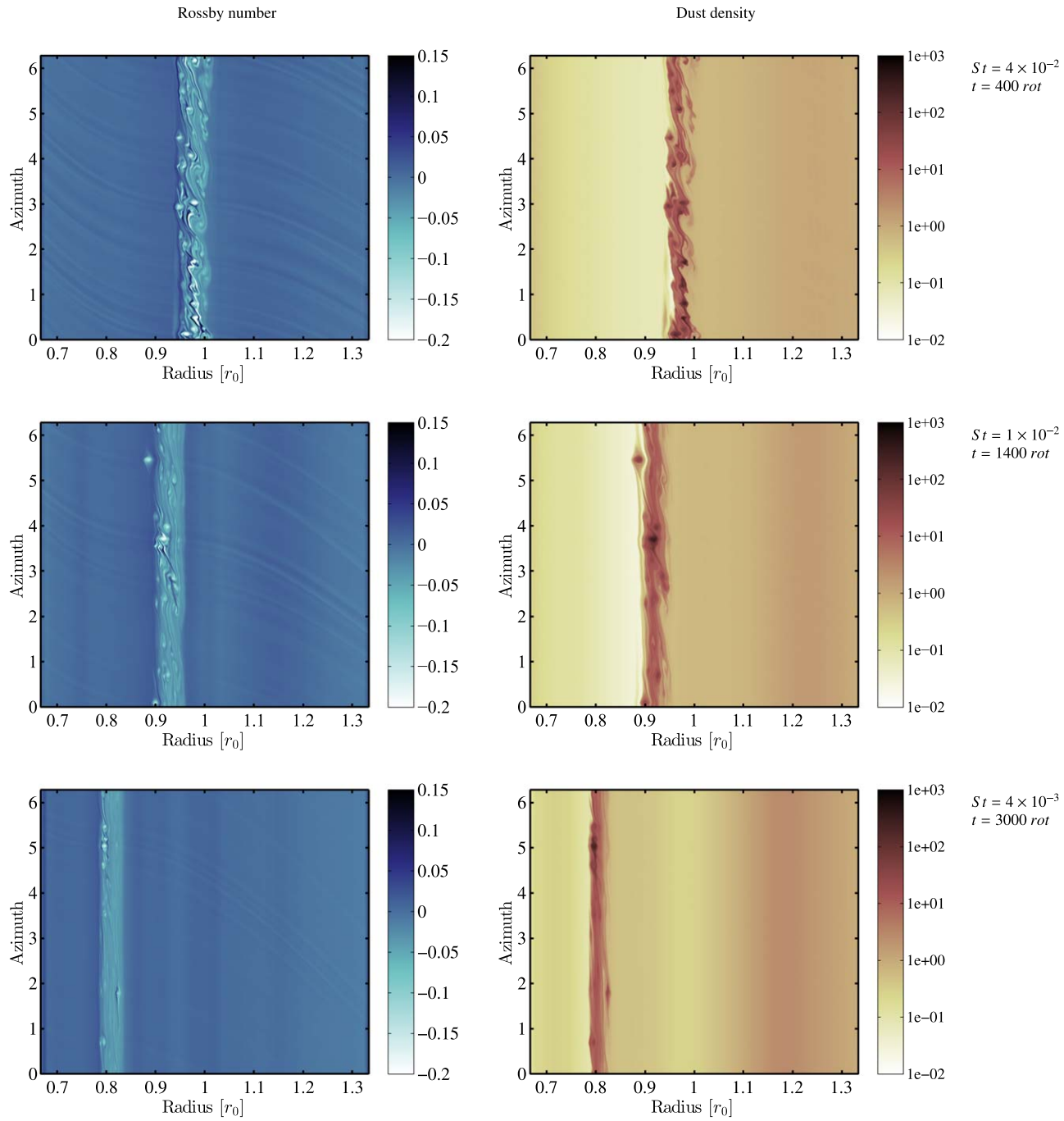

Figure 10. Comparison of the structure of the dusty ring for different grain sizes. We show snapshots of the main runs after the formation of the dust ring. From top to bottom: the grain sizes correspond to $St = 4 \times 10^{-2}$, $St = 1 \times 10^{-2}$, and $St = 4 \times 10^{-3}$, respectively. The last main run is not included because no dust ring is formed at the end of the simulation. We report the (r, θ) maps of the Rossby number on the left, and we show the maps of the dust density in a logarithmic color scale on the right.

generation of new small vortices. As in the case with $St = 10^{-2}$, a solitary dusty eddy was formed during the phase of the vortex destruction, and it survived during the dust ring formation. Despite the fewer number of eddies, the dust-to-gas ratio reached in the surviving eddy was 5.

One of the outcomes of this comparison is that diffusion in the flow, numerical in our case, has a strong impact on the evolution of the dust ring. The use of a medium resolution in the main runs, $(N_r, N_\theta) = (1024, 2048)$, not only produces significant numerical diffusion, but also limits the resolved scale length of the flow. As the size of the dusty eddies in the dust ring seems to reduce when the Stokes number decreases, the convergence with resolution is crucial. We show in Figure 11 the evolution of the dust ring that we obtained in the high-resolution run, with $St = 4 \times 10^{-3}$, and $(N_r, N_\theta) = (2048, 4096)$.

When we zoom-in the radial dimension to reveal the details of the flow, we clearly see that using a higher resolution resolves the dusty eddies far better. A dozen small-scale dusty vortices survive over hundreds of disk rotations, with a local dust-to-gas ratio higher than 0.1. The differentiation from the wide dusty bump is more prominent. If the resolved scale is

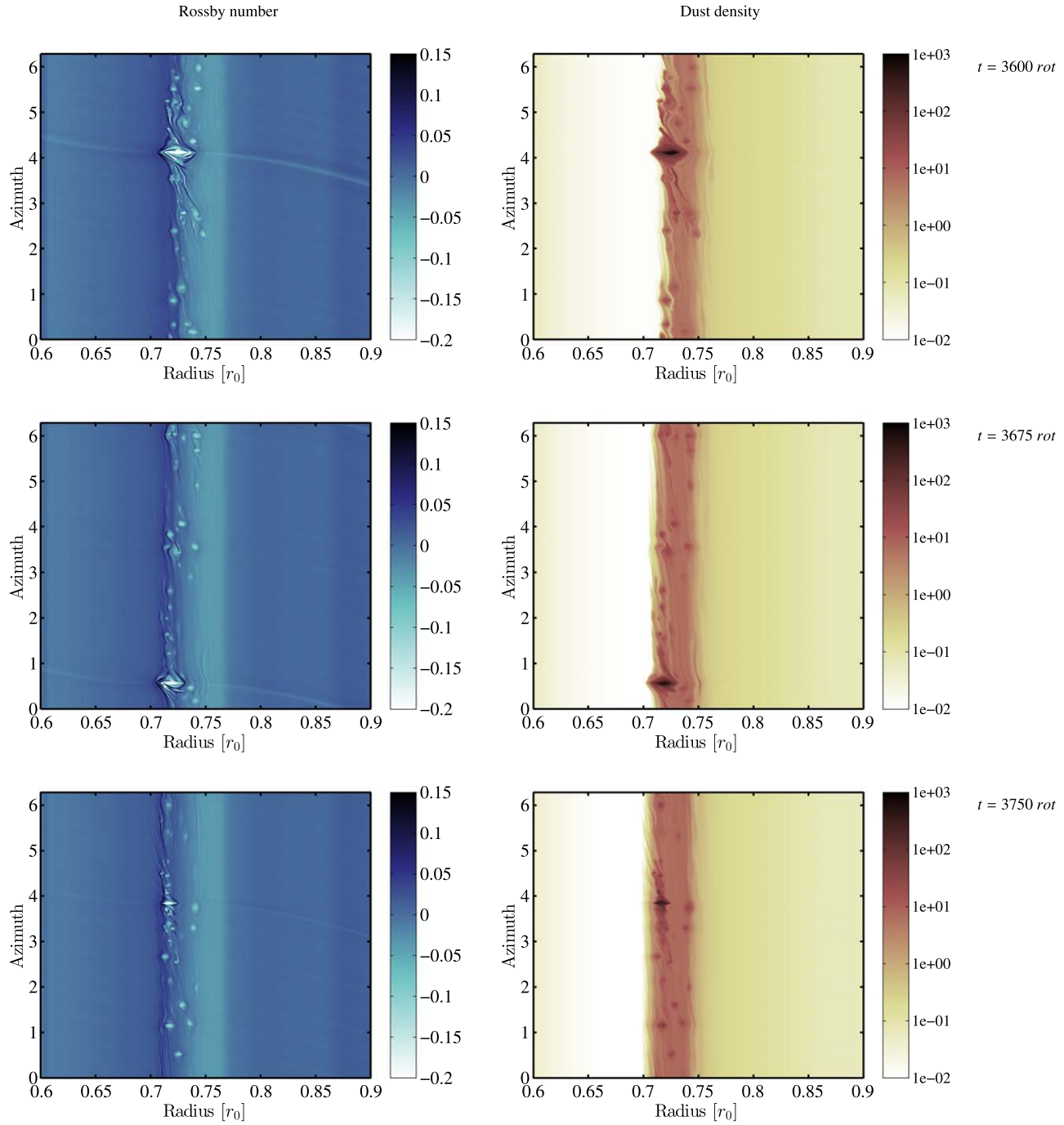

Figure 11. Late evolution of the dusty ring for the high-resolution additional run, with $St = 4 \times 10^{-3}$. From top to bottom: snapshot at $t = 3600$, $t = 3675$, and $t = 3750$ rotations, respectively. We report the (r, θ) maps of the Rossby number on the left and the maps of the dust density in a logarithmic color scale on the right. The maps are zoomed in radially to reveal the details of the structures in the flow.

smaller in this high-resolution run, allowing us to follow these small eddies, it is still difficult to sustain turbulence by the drag instability, like with larger grains. In fact, the drag timescale is typically of order $\sim$1000 orbits, which is of the order of the numerical diffusion timescale.

The vortex remnant with the largest amount of dust is stronger at higher resolution. At $t = 3600$ disk rotations, shown in the top row, this dusty structure even excites density waves that are visible in the Rossby number map (left). The size of this dusty eddy eventually shrinks to smaller scales, which releases some solid material to the dust ring in the form of smaller eddies. However, despite the decrease in density, the dust-to-gas ratio stays much higher than unity, indicating a new interesting path to confine dust to gravitational instability. This beyond the scope of this study, however.

The evolution of the maximum dust-to-gas ratio during the high-resolution run is presented in the top panel of Figure 12, and a map obtained at $t = 3750$ disk rotations in the bottom panel. Even with a Stokes number of 4×10^{-3}, the highest dust-to-gas ratio obtained during the evolution of the vortex is much higher than unity. During the first thousand orbits, the dust is accumulated inside the vortex, as described earlier.

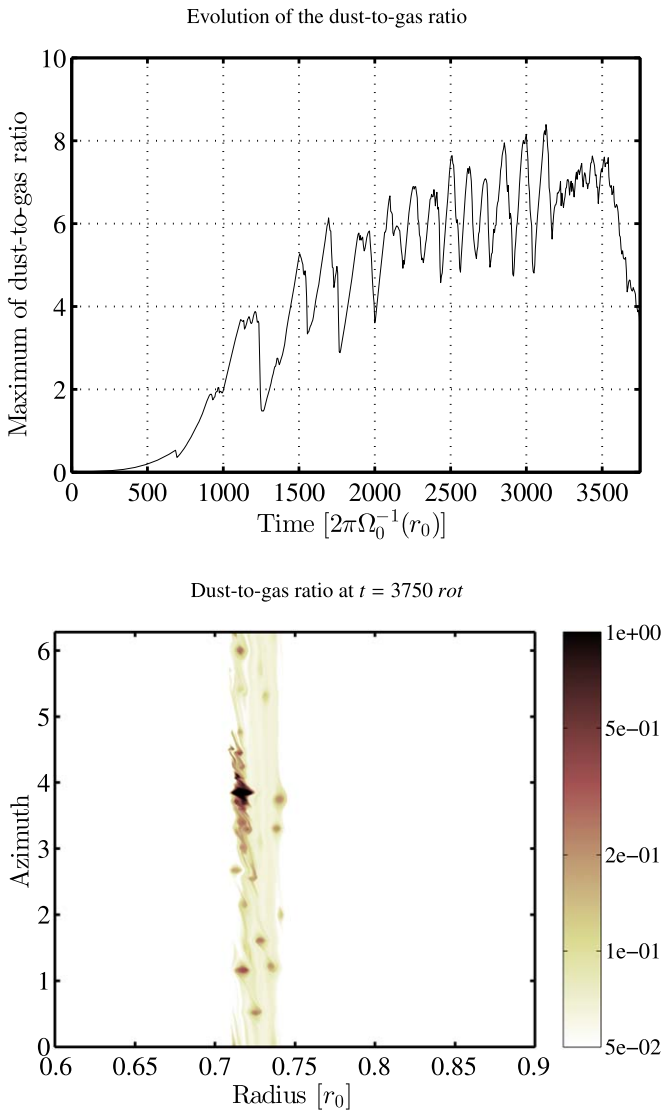

Figure 12. The local dust-to-gas ratio for the high-resolution run, with $St = 4 \times 10^{-3}$. Top: evolution of the maximum of the local dust-to-gas ratio in the disk. After about 1500 rotations of the disk, the highest value is much higher than unity, typically in the range 5–8. Bottom: map of the dust-to-gas ratio σ_p/σ_g at the end of the run, i.e., $t = 3750$ rotations.

During the unstable evolution of the vortex, however, for $1500 < t < 3200$ disk rotations, the dust confined in the vortex core reaches dust-to-gas ratios that on average increase from 4 to 7, and some peaks even up to 8. This period may favor for dust grain growth and gravitational instability because the dust density is very high. On the other hand, the unstable nature of the dusty vortex can counteract these processes.

However, from $t = 3200$ disk rotations to the end of the run, the dust ring is formed and the last compact eddy survives and shrinks, as explained previously. This period can be more favorable for the cited processes because the dynamics of the dust in this large eddy is more quiet. The steady value of the dust-to-gas ratio around 7 sustained for $3200 < t < 3500$ is a signature of this aspect. Later on, the dust-to-gas ratio linearly decreases to 4 at the end of the run, while the size of the eddy shrinks. The state of the disk at the end of the run, shown in the bottom panel, shows that even if this extreme value is localized, the rest of the dust ring still corresponds to a dust enhancement higher than 10. In the smaller eddies, the dust-to-gas ratio is higher than 0.2.

The formation of a dust ring is a common outcome of the destruction of dusty vortices and was observed in our runs for Stokes numbers down to $St = 4 \times 10^{-3}$. However, the impact of this structure on the dust dynamics and on possible paths toward planetesimal formation differs for different grain sizes. The larger grains, typically with $St > 10^{-2}$, sustain turbulence and generation of new dense eddies, as described in Surville et al. (2016). It is the most active phase that is observed after the vortex instability. For this population, the dust ring evolution is most favorable for grain growth and eventually gravitational collapse because of the high dust densities, the small size of the eddies, and the confinement, which might reduce collisional velocities. It is also a long-lasting phase of the disk evolution, which provides an opportunity for these processes to occur. Finally, a signature of these large grains is the large number of small dense eddies that survives, which represents a possible path for forming asteroid belts.

The well-coupled grains, with $St < 10^{-2}$, however, interact with the gas on timescales that are too long to sustain a turbulent flow in the dust ring. The evolution of the eddies is quiet and sensitive to different forms of diffusion acting on timescales comparable to $1/St$ rotations. During the dust ring phase, the small solid material is passive and evolves in a small number of eddies. Their density is not high enough to expect gravitational collapse to occur, but grain growth is possible due to low collisional velocities produced by the small amount of turbulence. Finally, a signature of these small grains is the isolated very dense eddy, a remnant of the vortex destruction, that could produce a large-size planetesimal if gravitational collapse starts.

5.4. The Crucial Concept of Timescale

In Section 4 we observed a repetition of instabilities in the disk when the Stokes number was smaller than approximately 10^{-2}. This phase lasts for a very long period, generating episodic events of strong mixing of gas and dust inside the vortex. To understand the origin of this effect, we analyze the $St = 4 \times 10^{-3}$ high-resolution run, just after the linear capture phase. Figure 13 shows the evolution of the Rossby number of the gas and of the dust density at four instants between $t = 685$ and $t = 740$ disk rotations. In the first row, we observe the nonlinear saturation of the vortex instability, with the dust following the unstable vortex core. The range of values of the dust density is restricted, however, with a high concentration at the vortex center. At $t = 700$ rotations in the second row, the instability has covered the whole vortex, and strong waves are excited from the inner parts, where the highest vorticity is located. The mixing of the gas due to the vortical motion is visible as spiraling stripes of vorticity all over the vortex. This mixing is mirrored in the solid phase of the flow. The dust density map, on the right, reveals that the grains have spread out over a large part of the vortex, forming filaments that indicate a turbulent event. A dense core where the dust density is an order of magnitude higher than in the rest of the vortex appears, superimposed on a high-vorticity core that is visible in the left panel.

The two last rows, at $t = 715$ and $t = 740$ rotations, respectively, illustrate the process of vortex relaxation. While the high-vorticity core remains at the vortex center, in which a dense clump of solids is embedded, the rest of the vortex

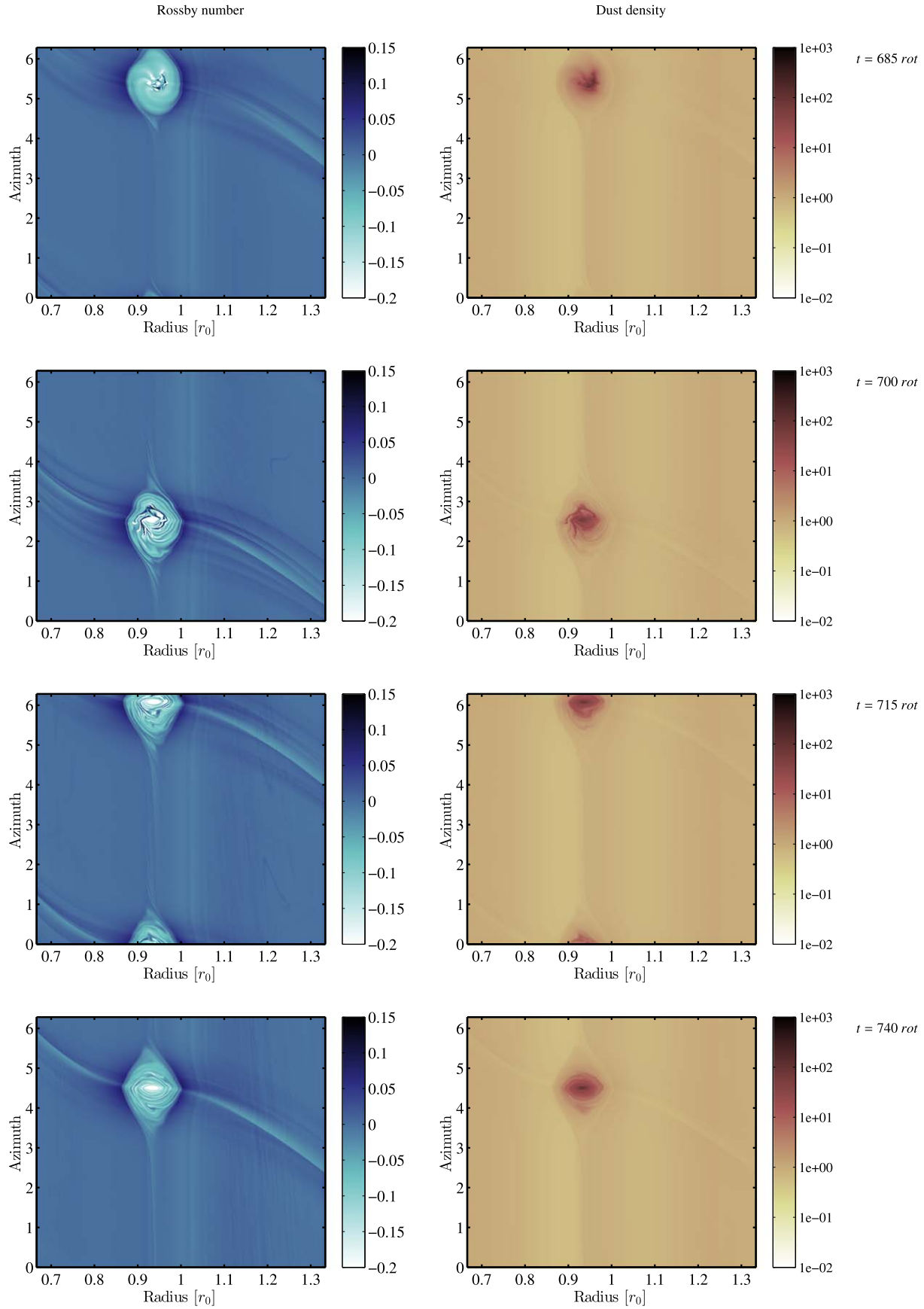

Figure 13. First vortex instability. We show the development of the instability after the linear capture observed in the high-resolution run, for $St = 4 \times 10^{-3}$. From top to bottom: Snapshot at $t = 685$, $t = 700$, $t = 715$, and $t = 740$ rotations, respectively. We report the (r, θ) maps of the Rossby number on the left and the maps of the dust density in a logarithmic color scale on the right.

reaches a smooth equilibrium. During this relaxation, the stripes of vorticity merge together toward the mean value of the vortex, $Ro \sim -0.13$. Because the coupling between gas and solids is strong, the dust follows this relaxation. The density profile, presented on the right, shows the formation of an extended region, where the dust density is more than 10 times higher than the initial value. During the vortex instability and this relaxation process, the dust that was compacted at the vortex center during the capture is strongly mixed inside the whole vortex, and then redistributed into two structures: (i) a dense small core, where the density is comparable to the density that was reached at the end of the capture, and (ii) a wide homogeneous patch that covers almost the entire vortex area and contains a significant fraction of the captured solid material. This second structure is thus a reservoir of material that after relaxation continues to be pushed toward the vortex center and that contributes to increasing the mass of the inner dense core.

The relaxation of the vortex is a hydrodynamical process that also occurs without dust. In fact, it is observed during the first 10 disk rotations when a Gaussian vortex model is used as an initial condition of the simulations. Vortices are in general in an equilibrium close to the geostrophic balance, as we discuss in Surville & Barge (2015). When a disturbance displaces the vortex profile from this quasi-equilibrium and no physical process sustains this disturbance, the vortex therefore relaxes back to the smooth equilibrium profile. The typical timescale of this rearrangement is the circulation period inside the vortex, which is related to the vorticity of the vortex, i.e., $\sim 1/|Ro|$. This gives an estimate in the range [5, 10] orbital periods for values of the Rossby number in the range $[-0.2, -0.1]$. This compares well with the results in Figure 13, where the vortex has strongly relaxed between $t = 700$ and $t = 715$ disk rotations.

In the case of a dusty vortex, the drag eventually changes the vorticity profile. The timescale of the effect on the vorticity is the same as the timescale of the dust capture because of the drag back-reaction, i.e., $\sim 1/St$. As a result, if the Stokes number of the dust grains is too small, then this timescale will be much longer than the relaxation of the vortex. When we assume the relaxation period to be 10 rotations, then an order-of-magnitude argument saying that the drag can be neglected when the timescale is 10 times longer, i.e., 100 rotations, gives a critical Stokes number of 10^{-2}. This reasoning is in agreement with the numerical results because we observe vortex relaxation after the first instability in the main run with $St = 10^{-2}$ (see Section 4.1).

After the relaxation, the capture of solids continues until the vorticity profile in the vortex again becomes unstable. When the accumulation of dust is strong enough to trigger the vortex instability again, the dust is distributed in a dense core at the vortex center and in an extended corona where the modes grow. Then the instability expands far from the vortex center, generating a chain of embedded vortices. The dust grains that were previously confined at the vortex center experience a strong mixing inside the vortex and are efficiently redistributed from the core to the corona. This effect can have a significant influence on the mechanisms of grain growth, in particular as concerns fragmentation and sticking, because these processes are fast, on timescales of the order of the local orbital period (Birnstiel et al. 2012).

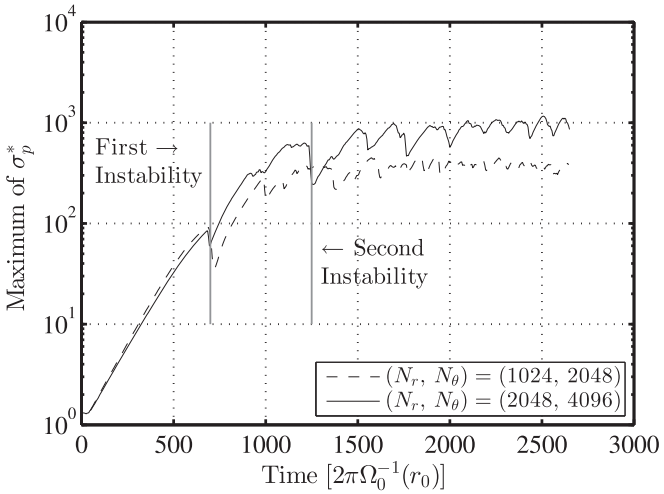

Figure 14. Identification of successive drag instabilities. We compare the evolution of the maximum of the dust density inside the vortex for the main run and the high-resolution run (dashed and solid lines, respectively), for the same setup with $St = 4 \times 10^{-3}$. We identify the first and second main vortex instabilities, which produce fast reductions of the maximum of the dust density.

If the vortex can still relax, a high-vorticity core forms at the center of the vortex. The area of this new core increases each time an instability event is triggered. The dust density inside the vortex increases strongly after each instability event. The vorticity at the vortex center also increases. As a consequence, each event of vortex instability reinforces the loading of dust in the vortex, reducing the timescale of the drag force, and also generates a less stable vorticity profile. As an outcome, the vortex cannot relax and an active dusty flow is sustained in its core, eventually leading to its disruption.

The recurrence of phases of instability during the vortex evolution is a new aspect of the dust-vortex interaction in the regime of well-coupled grains. It can be identified and traced by inspecting the evolution of the maximum dust density, as seen in Figure 14. We show in this figure the time evolution of the maximum of the dust density (solid line) for the high-resolution run with $St = 4 \times 10^{-3}$. From the initial time to $t = 700$ disk rotations, the initial linear capture of dust is at play, with an exponential growth of the density, as discussed in Section 4.1. The first time the vortex instability grows is identified on the plot. There is a significant reduction of the maximum dust density, in a very short period, corresponding to the relaxation of the unstable vortex. Then a second phase of capture, with an exponential growth of the dust density, starts, and this lasts until $t = 1100$ rotations. The growth rate is similar to the rate of the first capture phase because the Rossby number in the vortex has the same value, i.e., $Ro \sim -0.13$, in particular in the dust corona, as discussed previously (see Figure 13).

After a stabilization of the maximum density, the instability is triggered for a second time, at $t = 1200$ rotations. The dust density is reduced by a factor two during the instability because of the reorganization of the distribution of the solids inside the vortex, as described previously. Later on, several phases of instability occur until $t = 2000$ disk rotations. Between these three additional events of instability, dust is accumulated at the same rate, until it reaches an enhancement of 10^3 times the background value. In this case with $St = 4 \times 10^{-3}$, it takes almost 2000 orbits and five instability phases to increase the

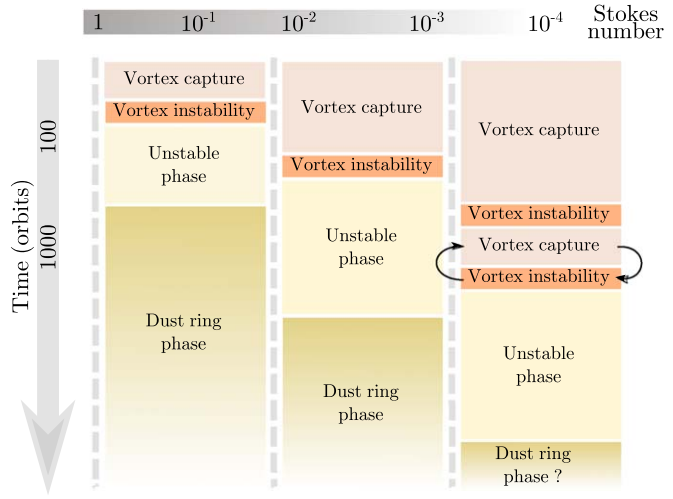

Figure 15. Schematic view of the evolution of a dusty vortex as a function of the grain size. The four main events during the evolution are identified with different colors. The time line on the left helps to visualize that the duration of the phases increases when the Stokes number is reduced. The values of St mentioned in the top bar are indicative, but we emphasize the critical difference between the $St > 10^{-3}$ and $St < 10^{-3}$ regimes. In the latter, the black arrows show the repetition of dust capture and vortex instabilities that we observe in this study. For too small dust grains, we were unable to obtain the formation of a dust ring before the end of the run.

maximum dust density up to 1000 times the background value, and to prevent the vortex from relaxing.

A comparison with the main run (dashed line) for the same grain size gives similar results. The growth rates are comparable, but the times corresponding to the onset of the unstable phases differ slightly from those in the high-resolution run after the first instability. The maximum dust density obtained at the end of the sequence is also reduced to 400 times the background value, and is more constant. This is due to the lack of spatial resolution, which filters out the high mode numbers of the instabilities. However, the same sequence of events and their related processes can be captured regardless of resolution, lending strong support to our general findings.

The competition between several processes, which are vortex instability, relaxation of the vortex to a new quasi-steady structure, dust drag effects during dust capture, and dust ring phases, governs the evolution of dusty vortices. The relative importance of each effect depends on the timescale of the underlying physics and changes during the whole evolution of the disk. In light of the results we obtained in this study, as well as in Surville et al. (2016), we designed a diagram that summarizes the different evolutionary pathways of the vortex as a function of the dust grain size (Figure 15).

The main aim of this cartoon is to highlight the different evolutionary phases we studied in this work, which are identified by different colors:

1. The dust capture phase in the vortex: this process occurs on a timescale of $\sim(\Omega_k St)^{-1}$,
2. the vortex instability phase: this develops on a short timescale on the order of Ω_k^{-1},
3. the unstable evolution phase: in competition with the drag, the typical timescale is the vortex relaxation $\sim$(1–10) $\times$ Ω_k^{-1},
4. the dust ring phase: the duration depends on the source of diffusion in the system (numerical, physical such as viscous stress effects).

For the largest dust grains, $1 < St < 10^{-3}$, that we can call weakly coupled grains, the four phases take place, and the system usually ends up in a long-lived turbulent dust ring. The global amount of time necessary to cover the whole evolution is related to the drag timescale and is therefore longer for smaller grains. However, the dust density enhancements to dust-to-gas ratios higher than unity is a common result that is weakly dependent on the Stokes number. The dust ring state is thus the most relevant for contributing in the process of planetesimal formation for these weakly coupled grains.

For the smallest dust grains, $St < \sim 10^{-3}$, which we refer to as well-coupled grains, a sequence of vortex instabilities and dust capture, graphically indicated by the curved arrows in Figure 15, is necessary to really destabilized the vortex and eventually transition to the dust ring phase. There is a continuous transition between behavior at varying Stokes numbers, so that the number of subsequent instability episodes increases as the Stokes number decreases. Furthermore, if the drag timescale is too long compared to the relaxation timescale of the vortex, the formation of a dust ring is unlikely. During the long-lived unstable phase, dust-to-gas ratios are higher than unity and are sustained during a very long period. It is thus the most relevant phase for contributing in the process of planetesimal formation for these well-coupled grains.

6. Conclusions

This study aimed at clarifying the effect of small well-coupled dust grains on the evolution of large-scale vortices in protoplanetary disks. Indeed, while we have shown in our previous work that grains with $St > 10^{-2}$ have a strong impact and produce turbulent dust rings with high dust-to-gas ratios, it was not clear whether smaller grains can have similarly strong effects on disk evolution. In particular, the formation of long-lived structures in which a large amount of dust is embedded has key implications on the development of other phenomena such as the SI, on grain growth models, and on the possibility of a direct gravitational instability of the dust layer, which are all possible pathways for planetesimal formation.

For a really wide range of Stokes numbers, corresponding to grains $\lesssim$mm -10 cm in size, depending on distance from the star in the disk, high dust density concentrations, with dust-to-gas ratios in the range 1–10, do arise one way or another. In one case because of dust capture and subsequent turbulence developing in the vortex when this is very long lived, as for the smallest grains. In the other case because a turbulent dust ring with multiple high dust concentration regions develops after the vortex dissipates relatively fast for the largest grains. Therefore the only required condition to lead to high concentrations of dust is that a vortex is somehow generated in the disk at some point and depends weakly on how this evolves subsequently. This is the main difference with previous works that have investigated vortices in dusty disks. However, when the vortex dissipates relatively fast and the dust ring develops afterward, which occurs preferentially for larger Stokes numbers, a qualitative difference arises in that a larger area of the disk is covered with prominent dust concentrations owing to the global nature of the ring as opposed to the initial local nature of the vortex. More specifically, we can summarize our findings as follows:

1. Because the drag force experienced by small dust grains is very strong, a specific implicit numerical scheme was

implemented in the code RoSSBi to accurately follow the dynamics of the disk. This method is very accurate for any value of the Stokes number of the pressureless dust fluid, and we use it to study the evolution a vortex model with dust characterized by Stokes numbers in the range $4 \times 10^{-2} < St < 10^{-3}$.

2. Dust is systematically accumulated inside the vortex for every value of the Stokes number. The exponential growth rate of the dust density at the vortex center follows the analytical model we developed in our previous study. The timescale depends on the grain size, but the density enhancement reached at the end, when the gas is perturbed by the drag force, is similar regardless of the Stokes number, and produces dust-to-gas ratios of order unity. We highlight the existence of a generic capture process, characterized by a timescale that scales with the Stokes number, which allows us to compare disks with different dust sizes at an equivalent state of evolution, but corresponding to intrinsically different physical timescales.
3. The vortex instability is triggered at the end of the capture, regardless of the grain size. The growth rates of the excited modes also depend weakly on the Stokes number. This effect is highly correlated with the similarity of the dust capture, and the concept of equivalent states of evolution, producing almost the same perturbation of the gas vorticity profile.
4. A new phase of dusty vortex evolution is discovered for Stokes numbers on the order of 10^{-3} and below, where a succession of vortex instabilities followed by dust capture events occurs. This period lasts several hundred of disk orbits and produces strong mixing and a fast reorganization of the dust during the relaxation of the vortex. The dust-to-gas ratio increases progressively to high values, up to 8 at the vortex center. The very dense core that forms and survives even after eventual vortex dissipation could be a preferential place for planetesimal formation.
5. When the timescale of the drag effect is too long compared to the resistance and relaxation of the vortex, the formation of a dust ring becomes unlikely. In our case, the runs with $St = 10^{-3}$ were still in the unstable phase by the end of the simulations. Even when it forms, for $St < 10^{-2}$, the dust ring produced by well-coupled grains has fewer eddies than with larger Stokes numbers. Even if the dust-to-gas ratios are comparable, they suffer diffusion, and their role in planetesimal formation is less promising than the unstable phase.

There are a number of caveats to our model that need to be pointed out. First, the fact that the simulations are still only two-dimensional, which could have a relevance both for the development of two-fluid turbulence during and after the vortex instability phase (see the discussion in Surville et al. 2016). We find that the instability and the active flow in the dust ring or in the vortex are efficient sources of dust diffusion for this class of non-turbulent compressible vortices.

However, some other vortices, a class of incompressible vortices with closed streamlines, may be sensitive to 3D turbulence driven by the elliptical instability. Finally, α turbulence of the disk , driven by MRI, the SI, or the VSI, could act as additional source of diffusion of the dust density. We will properly investigate the competition between the diffusion of the two-fluid instability and other sources of turbulence in a full 3D study in an upcoming publication.

Related to this aspect, the only source of dissipation in our models is the numerical diffusion. However, we showed that we have enough resolution to capture the instability and the active flow in the dust ring in a converged manner regarding the resolution. Similarly to the SI, the instabilities we observe in our runs need a high resolution (and a low diffusion) to be captured. As a last argument, the α viscosity expected in the disk is as low as 10^{-4}–10^{-5}, which corresponds to diffusion timescales much longer than the duration of our runs.

Second, the absence of self-gravity of the dust, which could play a role as soon as the dust-to-gas ratio locally increases above unity, and may trigger gravitational collapse. Finally, the fact that the dust size is fixed in each individual simulation as we did not include a prescription for the coagulation and fragmentation of grains. Concerning this last point, it is important to note that in addition to the mixing processes that occur during the unstable evolution of the vortex, the dense dust eddy surviving can be a favorable place for grain growth processes. If the mean grain size increases, then the Stokes number of the dust will also increase, and the evolution path of the system will move to the left in the diagram shown in Figure 15 even for grains with initially very small Stokes number. This means that destabilization of the vortex will be stronger and the probability to form a turbulent dust ring would increase. Because when the grains become larger, their evolution toward high concentrations is faster and most efficient owing to the formation of the turbulent ring, the implication would be that even very small dust grains, such as primordial dust, could evolve rapidly toward the formation of multiple dense eddies, and thus planetesimals. This hypothesis has to be confirmed with simulations including the different processes relevant to dust grain evolution. In a companion paper (Tamfal et al. 2018), we present the first results of a new subgrid method that can indeed model coagulation and fragmentation of grains, thus including a variable grain size in the code RoSSBi. The new method will be applied soon to simulation setups analogous to those presented in this work.

This work has been carried out within the frame of the National Center for Competence in Research *PlanetS* supported by the Swiss National Science Foundation (SNSF). The authors acknowledge the financial support of the SNSF. Numerical simulations were performed on the *Piz Daint* Cray XC50 system of the Swiss National Supercomputing Center (CSCS). C. Surville would like to thank M. Hutchison for his usefull comments and corrections to the draft.

ORCID iDs

Clément Surville https://orcid.org/0000-0001-8998-7267

References

Andrews, S. M., Wilner, D. J., Zhu, Z., et al. 2016, ApJL, 820, L40
Barge, P., Ricci, L., Carilli, C. L., & Previn-Ratnasingam, R. 2017, A&A, 605, A122
Birnstiel, T., Klahr, H., & Ercolano, B. 2012, A&A, 539, A148
Booth, R. A., Sijacki, D., & Clarke, C. J. 2015, MNRAS, 452, 3932
Brogan, C. L., Pérez, L. M., Hunter, T. R., et al. 2015, ApJL, 808, L3
Bryden, G., Beichman, C. A., Carpenter, J. M., et al. 2009, ApJ, 705, 1226
Chatterjee, S., & Tan, J. C. 2014, ApJ, 780, 53
Fu, W., Li, H., Lubow, S., Li, S., & Liang, E. 2014, ApJL, 795, L39

Gonzalez, J.-F., Pinte, C., Maddison, S. T., Ménard, F., & Fouchet, L. 2012, A&A, 547, A58
Gras-Velázquez, À., & Ray, T. P. 2005, A&A, 443, 541
Hopkins, P. F., & Squire, J. 2018, MNRAS, 480, 2813
Jacquet, E., Balbus, S., & Latter, H. 2011, MNRAS, 415, 3591
Johansen, A., & Klahr, H. 2005, ApJ, 634, 1353
Johansen, A., & Youdin, A. 2007, ApJ, 662, 627
Johansen, A., Youdin, A. N., & Lithwick, Y. 2012, A&A, 537, A125
Kowalik, K., Hanasz, M., Wóltański, D., & Gawryszczak, A. 2013, MNRAS, 434, 1460
Lambrechts, M., Johansen, A., & Morbidelli, A. 2014, A&A, 572, A35
Lesur, G., & Papaloizou, J. C. B. 2009, A&A, 498, 1
Levison, H. F., Kretke, K. A., & Duncan, M. J. 2015, Natur, 524, 322
Lin, M.-K., & Youdin, A. N. 2017, ApJ, 849, 129
Lyra, W., & Lin, M.-K. 2013, ApJ, 775, 17
Meheut, H., Casse, F., Varniere, P., & Tagger, M. 2010, A&A, 516, A31
Meyer, M. R., Carpenter, J. M., Mamajek, E. E., et al. 2008, ApJL, 673, L181
Paardekooper, S.-J., Lesur, G., & Papaloizou, J. C. B. 2010, ApJ, 725, 146
Pérez, L. M., Isella, A., Carpenter, J. M., & Chandler, C. J. 2014, ApJL, 783, L13
Schäfer, U., Yang, C.-C., & Johansen, A. 2017, A&A, 597, A69
Sierra, A., Lizano, S., & Barge, P. 2017, ApJ, 850, 115
Simon, J. B., Armitage, P. J., Li, R., & Youdin, A. N. 2016, ApJ, 822, 55
Smith, R., Wyatt, M. C., & Dent, W. R. F. 2008, A&A, 485, 897
Squire, J., & Hopkins, P. 2018, MNRAS, 477, 5011
Surville, C., & Barge, P. 2012, arXiv:1201.3257
Surville, C., & Barge, P. 2013, EPJ Web Conf, 46, 05002
Surville, C., & Barge, P. 2015, A&A, 579, A100
Surville, C., Mayer, L., & Lin, D. N. C. 2016, ApJ, 831, 82
Tamfal, T., Drążkowska, J., Mayer, L., & Surville, C. 2018, ApJ, 863, 97
Yang, C.-C., & Johansen, A. 2016, ApJS, 224, 39
Youdin, A., & Goodman, J. 2005, ApJ, 620, 459
Youdin, A., & Johansen, A. 2007, ApJ, 662, 613
Youdin, A. N. 2011, ApJ, 731, 99
Zhu, Z., Stone, J. M., Rafikov, R. R., & Bai, X.-N. 2014, ApJ, 785, 122